INTERPRETING STRESS WAVE SIGNALS IN ROCK DRILLING SYSTEMS

Lappeenranta-Lahti University of Technology LUT

Master's Program in Computational Engineering, Master's Thesis

2023

Henri Ropponen

Examiners: D.Sc. (Tech.) Jukka-Pekka Uusitalo
Professor Bernardo Barbiellini

ABSTRACT

Lappeenranta-Lahti University of Technology LUT
School of Engineering Science
Computational Engineering
Technical Physics

Henri Ropponen

Interpreting stress wave signals in rock drilling systems

Master's Thesis
2023
75 pages, 37 figures, 21 tables, 1 appendix
Examiners: D.Sc. (Tech.) Jukka-Pekka Uusitalo and Professor Bernardo Barbiellini

Keywords: stress waves, rock drilling, strain gauge, finite element method

One of the most common ways to drill a borehole to rock, is to use percussion drilling which is based on frequently transferring high kinetic energies from the piston to the rock. When the piston collides with the shank, there will be a high magnitude stress wave propagating towards the rock. With the high stresses, the goal is to break the rock's structure which eventually creates a borehole. The challenge in percussion drilling is to minimize stress waves that reflect from the rock as they may be harmful for the system. Conventionally, stress waves are measured with strain gauges that measure the strain in an object. In elastic regime, this strain can be converted into stress with the help of Young's modulus. This Master's Thesis researches the possibility of configuring numerical Finite Element Method (FEM) models to gain stress wave data without the need of using strain gauges. The models are done for two different drilling systems of which there are strain gauge data available. For analysing the reflected waves in different rock conditions, the models use different parameters in the rock model. From the results it can be concluded that the incident stress wave can be simulated accurately if the model itself is accurate. The reflected stress wave cannot be predicted due to ever-changing rock conditions but it can be fitted with the help of measurement data.

TIIVISTELMÄ

Lappeenrannan-Lahden teknillinen yliopisto LUT
School of Engineering Science
Laskennallinen tekniikka
Teknillinen fysiikka

Henri Ropponen

Kallioporakoneen tuottaman jännitysaallon signaalin tulkitseminen

Diplomityö
2023
75 sivua, 37 kuvaa, 21 taulukkoa, 1 liite
Ohjaajat: TkT Jukka-Pekka Uusitalo ja Professori Bernardo Barbiellini

Avainsanat: jännitysaalto, kallioporaus, venymäliuska, elementtimenetelmä

Yksi tyypillisimmistä tavoista porata kolo kallioon on käyttää iskuporausta, joka perustuu toistuvien suurien kineettisten energioiden siirtämiseen männältä kallioon. Kun mäntä törmää niskaan, korkean suuruusluokan jännitysaalto kulkeutuu kohti kiveä. Korkeilla jännityksillä tavoitellaan kiven rikkomista, joka lopulta luo porareiän. Eräs haaste iskuporauksessa on minimoida jännitysaaltoja, jotka heijastuvat kiveltä, koska ne saattavat olla haitallisia järjestelmälle. Tavanomaisesti jännitysaaltoja mitataan venymäliuskoilla, jotka mittaavat kappaleessa esiintyviä venymiä. Elastisessa olosuhteessa tämä venymä voidaan muuntaa jännitykseksi kimmokertoimen avulla. Tämä diplomityö tutkii mahdollisuutta konfiguroida numeeristen elementtimenetelmien malleja jännitysaaltodatan tuottamiseksi ilman tarvetta käyttää venymäliuskoja. Mallit tehdään kahdelle eri porausjärjestelmälle, joista on olemassa venymäliuskadataa. Heijastuneiden aaltojen analysoimiseksi erilaisissa kiviolosuhteissa mallit käyttävät vaihtelevia parametreja kivimallissa. Tuloksista voidaan johtaa, että menevä jännitysaalto voidaan simuloida tarkasti, jos malli itsessään on tarkka. Heijastunutta jännitysaaltoa ei voida ennustaa alati muuttuvien kiviolosuhteiden takia, mutta se voidaan sovittaa mittausdatan avulla.

ACKNOWLEDGEMENTS

As the journey of this Master's Thesis is steadily coming to an end, I would like to thank all the colleagues at Sandvik who made the past months to feel like a stress free experience as every day at the office started with unpredictable and long-lasting coffee sessions. From Sandvik, I want especially to thank Jussi Peurala, Juha Pölönen, Teemu Rovio, and Tomas S. Jansson for the collaboration and creating the numerical models and data that I could use. In addition, from Sandvik, I sincerely thank Pasi Hämäläinen and my supervisor Jukka-Pekka Uusitalo whose many years of experience in the field could not be matched with. Last but not least, having Bernardo Barbiellini as the examiner from LUT was one of the key points to thrive a wide range of ideas to the thesis.

Besides the Master's Thesis itself, I feel grateful for not only choosing LUT University as the home university but also choosing this field of studies that has provided me a great mixture of technical physics and software engineering.

Even though the past five years have gone by so quickly, I am happy that the long-awaited time of graduation is nearly there and the work that I have done is slowly about to pay off. To quote my father, *"elefantti syödään pala kerrallaan"*.

Lappeenranta, February 21, 2023

Henri Ropponen

LIST OF ABBREVIATIONS

ΔL	Change in length
ΔR	Change in resistance
Δt	Time step
Δt_e	Time difference error
ε	Strain
ε_{axial}	Axial strain
ε_{trans}	Transverse strain
η	Stress wave efficiency
γ	Unloading parameter
ν	Poisson's ratio
ρ	Density
σ	Stress
σ_i	Incident stress wave
σ_c	Compressive stress
σ_r	Reflected stress wave
$\sigma_{r,b}$	Reflected stress from drill bit
$\sigma_{r,c}$	Reflected compressive stress
$\sigma_{r,t}$	Reflected tensile stress
σ_s	Shear stress
σ_t	Tensile stress
σ_{tr}	Transmitted stress
σ_x	Stress along x-axis
A	Cross-sectional area
B_m	Bulk modulus
$\mathbf{B}$	FE system strain matrix in global coordinate system in global coordinate
C	Correlation
C_i	Correlation of incident wave
C_r	Correlation of reflected wave
C_s	Stiffness
c	Speed of sound
c_e	Damping constant
c_{sg}	Speed of sound of strain gauge measurement
c_{sim}	Speed of sound of simulation
$cov(X, Y)$	Covariance
$\mathbf{D}$	FE system displacement matrix in global coordinate
$\ddot{\mathbf{D}}$	FE system acceleration matrix in global coordinate

$\mathbf{D}_e$	Element displacement vector in global coordinate
$\dot{\mathbf{D}}_e$	Element velocity vector in global coordinate
$\ddot{\mathbf{D}}_e$	Element acceleration vector in global coordinate
$\mathbf{D}_{t+\Delta t}$	FE system displacement matrix at time $t + \Delta t$ in global coordinate
$\mathbf{D}_{t-\Delta t}$	FE system displacement matrix at time $t - \Delta t$ in global coordinate
$\dot{\mathbf{D}}_{t+\Delta t}$	FE system velocity matrix at time $t + \Delta t$ in global coordinate
$\ddot{\mathbf{D}}_t$	FE system acceleration matrix at time t in global coordinate
$\mathbf{d}_e$	Element displacement vector
$\ddot{\mathbf{d}}_e$	Element acceleration vector
E	Young's modulus
$\mathbf{E}$	FE system Young's modulus matrix in global coordinate
E_σ	Stress wave energy
$E_{\sigma,i}$	Incident stress wave energy
$E_{\sigma,r}$	Reflected stress wave energy
F	Force
$\mathbf{F}$	FE system force vector in global coordinate
F_c	Compressive force
$\mathbf{F}_e$	Element force vector in global coordinate
$\mathbf{F}^{int}$	Initial force vector
$\mathbf{F}^{residual}$	Residual force vector
F_s	Tensile force
F_t	Uniaxial force
$\mathbf{f}_e$	Element force vector
G	Shear modulus
GF	Gauge factor
$\mathbf{K}$	FE system stiffness matrix in global coordinate
$\mathbf{K}_e$	Element stiffness matrix in global coordinate
k	Spring constant
$\mathbf{k}_e$	Element stiffness matrix
k_1	Loading spring constant
k_2	Unloading spring constant
L	Length
L_p	Piston length
$\mathbf{M}$	FE system mass matrix in global coordinate system in global coordinate
$\mathbf{M}_e$	Element mass matrix in global coordinate system
$\mathbf{m}_e$	Element mass matrix
$\mathbf{N}$	FE system shape function matrix in global coordinate
n	Number of samples

p'	Change in pressure
p_p	Percussion pressure
R	Resistance
$RMSE$	Root Mean Square Error
$RMSE_i$	Root Mean Square Error of incident wave
$RMSE_r$	Root Mean Square Error of reflected wave
S	Compliance
s	Distance
$\mathbf{T}$	Transformation matrix
T_d	Duration of incident wave
t	Time
t_0	Integral time limit start
t_1	Integral time limit end
U_{in}	Input voltage
U_{out}	Output voltage
u'	Change in velocity
V	Volume
V'	Change in volume
$Var(X)$	Variance
v	Particle velocity
W_σ	Work done by stress wave
x	Displacement
x_i	Observation of variable x
$\hat{x}_i$	Prediction of variable x
$\partial x/\partial t$	Time derivative of displacement
Z	Mechanical impedance

CAD	Computer Aided Design
DTH	Down-The-Hole
FEA	Finite Element Analysis
FEM	Finite Element Method
LSM	Lattice spring model
THD	Top Hammer Drilling
1D	One-dimensional
2D	Two-dimensional
3D	Three-dimensional

CONTENTS

1 INTRODUCTION

1.1 Background

In percussion drilling systems, stress waves play a crucial role as the energy from the piston needs to be transferred to the breaking of the rock. This Master's Thesis interprets the stress waves in rock drilling systems by analysing stress wave data gathered from strain gauges. Commonly, stress wave data is used to tune the drill system to achieve higher energy efficiency and longer durability for the power transmission parts. To achieve a more precise analysis of the occurring stress waves, finite elements models are created and the resulting numerical data are compared with the measurements.

1.2 Objectives and delimitations

This thesis aims to study if simulated can models be tuned to correspond to strain gauge measurements. To achieve more in-depth research in this thesis, the following delimitations are in-place:

1. Numerical experiments are conducted only for a small batch of different drilling equipment.
2. Only existing rock drilling parts are used, i.e. no new ones are designed.
3. Material properties are chosen according to prior experiments and are not measured within this thesis.

1.3 Structure of the thesis

The thesis is divided into six sections, excluding this introduction. The first section focuses on reviewing literature and related works that can be used as a reference in this thesis. The second section presents the fundamentals of stress wave physics and how the underlying physics can be applied in measurement devices or numerical models. In addition, the theory section includes common statistical methods that are used to compare the results with each other.

Then follows the material and software section which focuses on giving the reader sufficient information about measurement devices, signal processing and software that are used to create numerical models of the drilling system. In the next section, the results obtained from the measurement devices and numerical models are presented. The last two sections focus on discussing the results and wrapping up the thesis with succinct conclusion.

2 LITERATURE REVIEW

This section gives an overview of studies that are related to this thesis. With the help of other studies, it is possible to come up with research methods that can be applied to solve presented research questions or use them as follow-up studies.

2.1 Stress wave propagation analysis with LS-DYNA

Kobayashi et al. [1] conducted a study that takes advantage of developing numerical models to research stress wave propagation in various experiments while validating the results with experimental data. For creating models, the study uses the software LS-DYNA that is based on the finite element method (FEM) approach. The FEM can be considered as one the of most popular and effective ways to numerically solve boundary value problems [2]. In the models, two cylindrical elastic bodies with different cross-sectional areas are being coupled to each other and one of these bodies experiences impacts from a striker. For viewing the mechanical changes in the system, stresses are being measured in two separate locations.[1]

By analysing stress wave propagation in elastic bodies, the study from Kobayashi et al. [1] wants to find an effective method that would reduce the magnitude of reflected stress waves that come from the tail end. In the study, two different sets of experiments are conducted. In the first set of experiments, a different connection type between the two bodies is researched. In the other set of experiments, the effect of varying output bar diameter and the insert length of the coupling is researched.[1]

To summarize the results from the study, any changes in the connection between the rods can have significant effects on the intensity of reflected stress waves [1]. While the models used in the study can be said to mimic percussion rock drilling, the system lacks a key component which is the rock model. Without the rock model, the incident stress wave in the second rod has nowhere to attenuate, thereby, it reflects back towards the striker.

2.2 Simulating rock drill impact with 3D FEM methodology

In a study from Chiang and Elías [3], the possibility of numerically modelling impact tools used in rock drilling is researched. In the study three different approaches were

taken to model the impact from the drill — these three being, impulse-momentum principle, 1D FEM, and 3D FEM. FEM analysis can be used in mining industry to simulate impact in stress-strain problems, to model post failure fracture propagation, and to examine material's linear properties.[3]

When comparing the three different approaches against each other with the addition of experimental data, all three methods can adequately simulate the impact from the rock drill. The 3D FEM approach is superior to 1D models when rock fragmentation is subject of the research. The cost of using 3D FEM models is their much longer computation run times which can take roughly forty times longer than the one with 1D FEM. The proposed method of using FEM analysis can be seen as suitable solution to numerically simulate the differences in energy transmission efficiency between two rock drills. It still should be noted that even the 3D FEM model is not suitable for accurately predicting the penetration rate of the drill.[3]

Even though the study from Chiang and Elías [3] was conducted for Down-The-Hole (DTH) drills, the proposed method of using numerical models proofs to have potential for solving the research problem with Top Hammer Drilling (THD) method used in this Master's Thesis.

3 THEORY

This part of the thesis goes more in depth with the theory and physics — giving enough information for the reader to understand the fundamentals of stress waves, how these stress waves can be measured or numerically computed and what type of statistical methods are used to evaluate the results.

3.1 Basic principles of percussion rock drilling

One common way to drill rocks is to use the THD method, where the rotation and percussion are realized outside the borehole. For the DTH method, the rotation takes place outside the borehole while the percussion is applied to the bit by the hammer or piston directly at the end of the rod. The main difference between these two methods is the type of energy transmission which makes them to have their own benefits in certain use cases. Usually, THD is used to drill smaller and shorter holes, while DTH can be used to drill longer holes due to more constant total efficiency which is not affected by the hole length that increases the energy losses for the THD method.[4] Commonly, DTH is used also for rocks that have a higher fragmentation. From this point forward, this thesis solely investigates rock drilling that uses the THD method.

The THD method relies on percussion drilling, where the main goal is to transfer the kinetic energy from the drill's piston to the rock frequently. At first the piston is accelerated hydraulically to a high speed, after which the piston collides with the shank adapter. At this stage, the piston's kinetic energy is transferred to the adapter and the collision of these two parts creates a stress wave. From the shank adapter, the incident stress wave travels through the drill rods towards the drill bit. When the incident stress wave has travelled to the end of the drill bit, there will normally be a reflected wave which travels back towards the drill.[4]

Figure 1 presents an overview image of a rock drilling system where the piston strikes the shank with a certain velocity which can be controlled with percussion pressure p_p. Upon the percussion, stress waves start to propagate towards the bit via a single or multiple rods. Once the stress waves reach the end of the bit, the bit will normally hit the rock, transferring some of its energy to the rock and thereby breaking the rock.

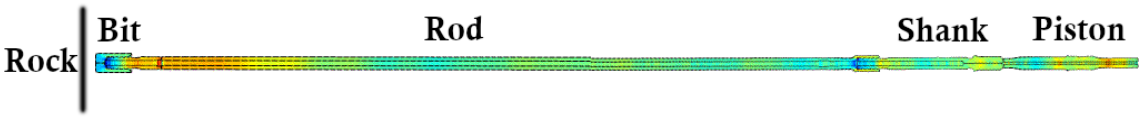

Figure 1. Overview image of a rock drill system.

In a case where the drill bit has a good contact with the rock, the incident stress wave makes the drill bit to hit the rock with high force. On the other hand, if the drill bit does not have a good contact with the rock, the incident stress wave has no place to absorb its energy — thereby, the wave reflects back towards the rock drill where there can be a stabilizer dampening parts of the energy from the reflected stress wave. If the reflected stress waves are not dampened by any means, the kinetic energy of stress waves eventually transforms into heat due to friction that is created by the interaction between the stress waves and the couplings.

3.2 Stress waves in rock drilling

Springs are one of the essential mechanical elements that can be used to describe energy absorption and storage. Mechanical properties of elastic materials can be described by Hooke's law, as in Equation (1), in which the required force F to compress or extend a spring is linear proportional to the spring's compression or extension x in its elastic regime. In Equation (1), the stiffness of the spring is denoted by k.[5] A system of springs can be traced back to atomic level. In crystallography, it is possible to model crystal structures with a lattice spring model (LSM), where the bonds between particles are presented as springs. By applying Newton's second law and Hooke's law, it is possible to numerically simulate structures under stress in an atomic level.[6][7] The Lorentz oscillator model shares the same approach of having mechanical mass-and-spring systems of electrons that carry energy in their moving masses, store energy in their springs, interact with local electromagnetic fields, and lose energy due to internal friction mechanisms.[8]

$$F = -kx \tag{1}$$

Materials that obey Hooke's law are called linearly elastic [9]. The elasticity is determined in form of the relationship between stress σ and strain ε. This relationship is described by

the Hooke's law which can be defined either with compliance S or stiffness C_s. Equations (2) and (3) show this relationship respectively for compliance S and stiffness C_s.[10]

$$\sigma = C_s \varepsilon \tag{2}$$

$$\varepsilon = S\sigma \tag{3}$$

If the stress σ and strain ε take place in an isotropic uniaxial case, the stiffness C_s can be presented by the Young's modulus E, as in the Equation (4) [10]. Since the strain ε is expressed as $\varepsilon = \Delta L/L$, where ΔL is the change in length and L is the initial length — Equation (4) can be rewritten to Equation (5) [11].

$$\sigma = E\varepsilon \tag{4}$$

$$\sigma = E\frac{\Delta L}{L} \tag{5}$$

The rock's ability to withstand external forces is directly proportional to the applied stress. Thereby, when interpreting the operation of rock drilling systems, it is important to analyse the stress waves that are generated from the percussion. In a simplified one-dimensional case, where the force F is applied to an object, the stress σ that the object experiences is defined by Equation (6), where A is the cross-sectional area of the object.[4]

$$\sigma = \frac{F}{A} \tag{6}$$

Concerning rock strength, the mechanical stress in Equation (6) can be divided into three different components of stress which are compressive stress σ_c, tensile stress σ_t and shear stress σ_s. These stresses are defined in Equations (7), (8) and (9) respectively, where F_c, F_t and F_s stands for a specific mode of applied force. Figure 2 illustrates in which direction the respective forces are applied in each case.[4]

$$\sigma_c = \frac{F_c}{A} \tag{7}$$

$$\sigma_t = \frac{F_t}{A} \tag{8}$$

$$\sigma_s = \frac{F_s}{A} \tag{9}$$

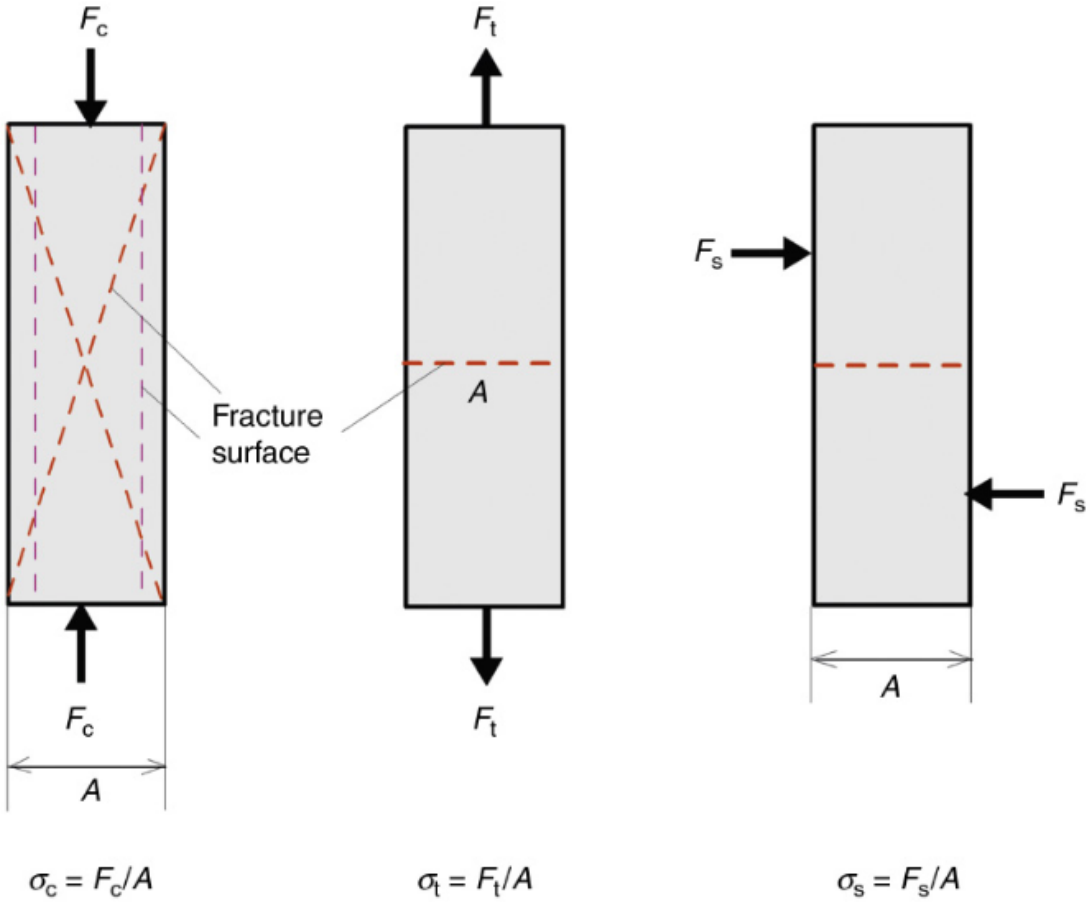

Figure 2. Compressive stress σ_c, tensile stress σ_t and shear stress σ_s. Figure reprinted with a permission from Elsevier.[4]

In terms of the strain ε, it can be axial ε_{axial} or transverse ε_{trans}, and the ratio between these is called Poisson's ratio $\nu = -\varepsilon_{trans}/\varepsilon_{axial}$. The Young's modulus E and Poisson's

ratio ν have the following relationship with each other

$$G = \frac{E}{2(1+\nu)}, \tag{10}$$

where G denotes the shear modulus of the material.[12]

In addition to the shear modulus G, bulk modulus B_m is used. The bulk modulus denotes material's ability to withstand changes in its volume, and it is defined as,

$$B_m = -V\frac{p'}{V'}, \tag{11}$$

where V is the initial volume, p' is the change in pressure, and V' is the change in volume. In Equation (11), the bulk modulus B_m describes the relation between applied pressure and relative deformation.[18]

3.2.1 One-dimensional stress wave theory

For more common and simplified system, stress waves can be illustrated in one-dimensional space. In such system, the following two assumptions can be made:

- The cross-sectional area of the drilling rod stays the same.
- All wave components travel at the same speed.

In reality the assumptions above are not valid, because the drilling rod's cross-sectional area changes at couplings and the wave speed is proportional to its frequency.[13] In the following studies [14], [15], [16], and [17], it has been stated that despite of having the previous assumptions, one-dimensional stress wave models can provide the desired accuracy for studying longitudinal stress waves in drilling rods.

When a stress wave encounters a point of discontinuity, it will be divided into two different components, those two being transmitted and reflected waves σ_{tr} and σ_r, respectively. The transmitted part of the wave travels through the discontinuity but the reflected wave reflects to the opposite direction of the incident wave. This phenomenon is demonstrated in

Figure 3, where coupled objects 1 and 2 have their individual densities ρ, cross-sectional areas A and Young's modulus E.[13] To determine the magnitude of the reflected and transmitted waves, changes in the mechanical impedances must be analysed. The mechanical impedance Z of system is defined in Equation (12), where p' is the change in pressure in given velocity change u' [18]

$$Z = \frac{p'}{u'}. \tag{12}$$

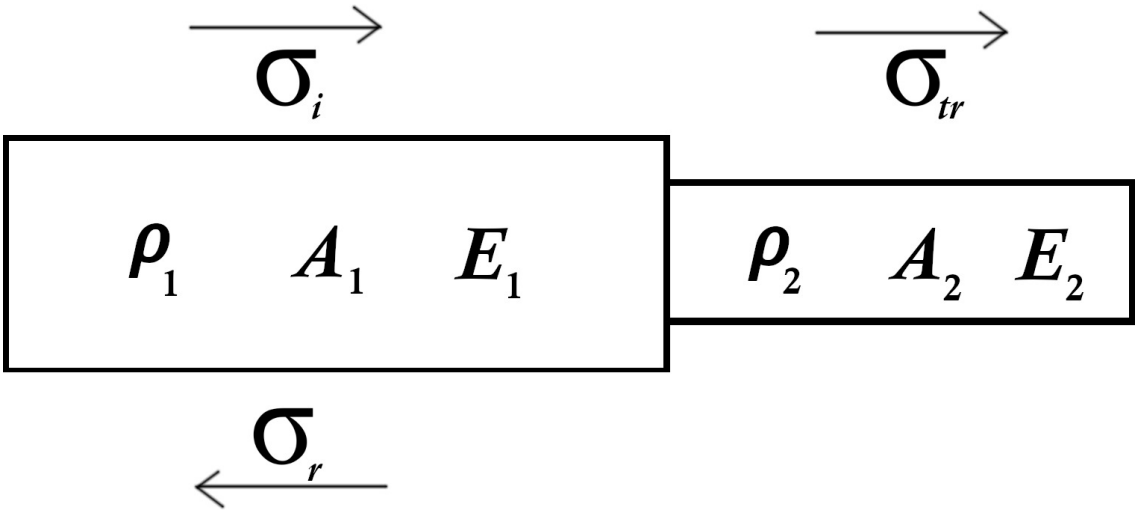

Figure 3. Incident σ_i, transmitted σ_{tr} and reflected stress σ_r waves at a point of discontinuity.

If the first object in Figure 3 moves towards the second object that is in rest, according to Equation (12), there will be an impedance mismatch. It is the impedance mismatch that transforms the incident wave into transmitted and reflected waves.[18]

At a point of discontinuity, as shown in Figure 3, the transmitted σ_{tr} and reflected waves σ_r are expressed respectively in Equations (13) and (14), where c is the speed of sound in a solid material [1][13][19]. The relationship between transmitted and reflected waves in Equations (13) and (14) derives from the impedances Z of the two objects and resulting in an impedance mismatch.

$$\sigma_{tr}(t) = \frac{2A_1\rho_1 c_1}{A_1\rho_1 c_1 + A_2\rho_2 c_2}\sigma_i(t) \tag{13}$$

$$\sigma_r(t) = \frac{-A_1\rho_1 c_1 + A_2\rho_2 c_2}{A_1\rho_1 c_1 + A_2\rho_2 c_2}\sigma_i(t) \tag{14}$$

If the objects in Figure 3 are homogeneous, meaning that their densities ρ and speeds of sound c are equal — Equations (13) and (14) can be reduced to Equations (15) and (16).

$$\sigma_{tr}(t) = \frac{2A_1}{A_1 + A_2}\sigma_i(t) \tag{15}$$

$$\sigma_r(t) = \frac{-A_1 + A_2}{A_1 + A_2}\sigma_i(t) \tag{16}$$

From Equation (16) it can be stated that the direction and magnitude of the reflected stress wave σ_r is dependent on the cross-sectional areas A_1 and A_2. By acknowledging these two dependencies, we can examine two distinctive cases, where $A_2 = \infty$ or $A_2 = 0$. When A_2 approaches infinity, it illustrates a case where the rod would be rigidly attached to the shank, as in,

$$\sigma_r(t) = \lim_{A_2 \to \infty} \left(\frac{-A_1 + A_2}{A_1 + A_2}\sigma_i(t) \right) = \sigma_i(t), \tag{17}$$

where the reflected σ_r has same magnitude as the incident σ_i [13]. On the contrary to Equation (17), a case with $A_2 = 0$, where there is no physical contact between the two objects results in Equation (18), in which the reflected wave σ_r has the same magnitude as incident σ_i but is in the form of tensile stress.[4][13]

$$\sigma_r(t) = \frac{-A_1 + 0}{A_1 + 0}\sigma_i(t) = -\sigma_i(t) \tag{18}$$

Concerning the transmitted wave σ_{tr} in Equation (15), it can be stated that, if the cross-sectional areas A_1 and A_2 are the same at the junction, the transmitted wave is equal to the incident wave

$$\sigma_{tr}(t) = \frac{2A_1}{A_1 + A_1}\sigma_i(t) = \frac{2A_1}{2A_1}\sigma_i(t) = \sigma_i(t). \tag{19}$$

In a case where two identical drilling rods are rigidly connected to each other by the end of the rods, Equation (19) states that the stress wave in the first rod must be equal to the one at the second rod after penetrating the junction.

3.2.2 Energy of stress wave

Stress wave energies can be analysed by estimating how much work W_σ a stress wave does. A well-known way of presenting work is by multiplying a force F with displacement x. From Equation (6), it is known that $F = A\sigma$. Thus, work W_σ can be expressed as:

$$W_\sigma = Fx = A\sigma(t)x, \tag{20}$$

where x denotes the particle displacement. Equation (20) also emphasizes that stress is a function of time. It is also known that displacement is a function of velocity and time, $x = vt$, where particle velocity v can also be expressed as

$$v = \frac{\sigma}{c\rho}, \tag{21}$$

where c is the speed of sound [4]. By applying $x = vt$ and Equation (21) to Equation (20), the work W_σ done by the stress wave is

$$W_\sigma = A\sigma(t)vt = A\sigma(t)\frac{\sigma(t)}{c\rho}t = \frac{A}{c\rho}t\sigma(t)^2, \tag{22}$$

where t expresses the period when the stress affects. With the speed of sound c in Equation (23), the work W_σ in Equation (22) can be rewritten in the form of Equation (24).

$$c = \sqrt{\frac{E}{\rho}} \tag{23}$$

$$W_\sigma = \frac{At}{\sqrt{\frac{E}{\rho}}\rho}\sigma(t)^2 \tag{24}$$

To better illustrate the effect of stress waves, the work W_σ will be denoted as energy E_σ. Since stress is a function of time in Equation (24), the change in energy over a period can be calculated by integration from time t_0 to t_1 which results in Equation (25) that can be used to calculate for example the energy of an incident wave

$$E_\sigma = \frac{At}{\sqrt{\frac{E}{\rho}}\rho} \int_{t_0}^{t_1} \sigma(t)^2 dt. \tag{25}$$

Energies of the incident and reflected waves are noted as $E_{\sigma,i}$ and $E_{\sigma,r}$ respectively. The stress wave efficiency η is calculated as

$$\eta = \frac{E_{\sigma,i} - E_{\sigma,r}}{E_{\sigma,i}}. \tag{26}$$

One of the biggest challenges in rock drilling is to transmit as much energy to the rock as possible [3]. With optimized drill rigs, it is possible to reach stress wave efficiencies of around 70-80 %. To give an example, if the kinetic energy of the incident wave is 360 J and 90 J get reflected, then the stress wave efficiency η corresponds to 75 %.

3.2.3 Compressive and tensile stress waves

When the rock drill piston collides with the shank, the shank experiences a force that is perpendicular to the piston's head — thereby, the force starts to compress the shank as in Figure 2, where the compressive stress is denoted as $\sigma_c = F_c/A$ [4]. To better illustrate the difference between compressive and elastic stress waves, Hooke's law can be re-formulated to:

$$\sigma = \mp \left(\frac{E}{c}\right) \frac{\partial x}{\partial t} = \mp \rho c \frac{\partial x}{\partial t}, \tag{27}$$

where the particle velocity $v = \partial x/\partial t$ can be positive or negative depending on the direction that the wave travels.[4] To solve Equation (27), initial values of stress σ and velocity v must be known. In a simplified case, where there is no stress initially applied and the particle velocity is zero, the solution of Equation (27) is

$$\sigma = \mp \rho c v. \tag{28}$$

When a stress wave propagates in the system with positive velocity v, negation in Equation (28) should be used for calculating negative stress that is compressive stress. On the other hand, tensile stresses are indicated with positive values in Equation (28).[4] Because in rock drilling, the goal is to apply compressive stress from the percussion to the rock, it is more natural to express compressive stresses as positive values and *vice versa* tensile stresses as negative values — thereby, from this point forward, in this thesis compressive stresses are expressed as positive values.

Figures 4, 5 and 6 show 2D-axisymmetric models of simplified rock drilling process. In these Figures, positive compressive stress waves σ_c are illustrated with blue colors and negative tensile stress waves σ_s with red colors. Figure 4 shows a cross-section view of rod, shank, and piston. In the upper image of Figure 4, the piston hits the shank, and the lower image shows moments later how the compressive incident stress wave starts to propagate left towards the drill bit.

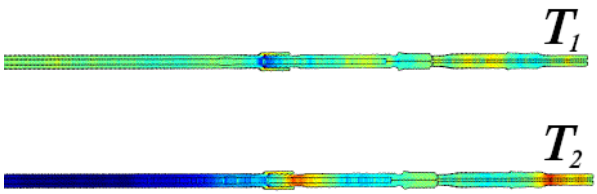

Figure 4. Incident stress wave propagating left at times T_1 and T_2, where $T_2 > T_1$.

The duration of the incident wave T_d in Figure 4 can be calculated as:

$$T_d = \frac{2L_p}{c}, \tag{29}$$

where L_p is the piston length and c is the speed of sound. Rearranging Equation (29) to $2L_p = T_d c$, shows that the length of the incident stress wave is twice as long as the piston length L_p.[20]

In upper images of Figures 5 and 6, the compressive incident stress wave is reaching the end of the drill bit and after a moment the wave reflects back towards the drill. The difference between Figures 5 and 6 are their initial conditions. In Figure 5 the drill bit and the rock have 1 mm gap but in Figure 6, there is no free space between those two. When comparing the reflected wave of these two cases, there is a notable difference in the reflected waves. The small gap in Figure 5 results in having high magnitude tensile stresses in the reflected wave. The full animation of Figure 6 is available in Appendix 1.

The reflected stress wave that travels back towards the drill should be minimized because its energy is harmful for the system — especially, for the threads that are used to connect bits, rods, or shanks. To maximize the drilling efficiency, the reflected stress waves should be prevented by pressing the drill bit to the rock.[11]

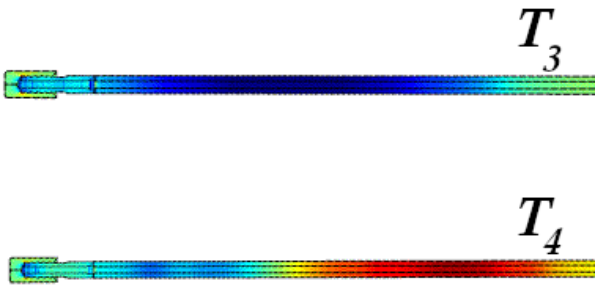

Figure 5. Incident stress wave propagating at time T_3. Reflected wave propagating at time T_4 after having a poor contact with the rock.

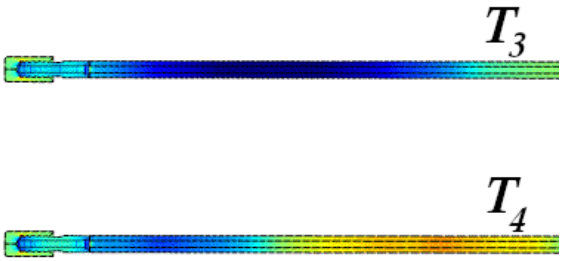

Figure 6. Incident stress wave propagating at time T_3. Reflected wave propagating at time T_4 after having a good contact with the rock.

3.2.4 Bilinear stiffness model of bit-rock interface

In addition to knowing the quality of the bit–rock contact, it is essential to know the rock properties. As the drill bit strikes the rock with a high force, the rock first experiences elastic deformation in form of strain. In the elastic regime, the deformation can be linear, nonlinear or a combination of both [21].

As atoms can be thought to function as a system of springs in material, it is possible to picture the energy transmission interface between the drill bit and the rock in form of springs. Figure 7 presents a Hookean bilinear stiffness model of bit-rock interface, where the stiffness k corresponds to the slope that is dependent on the direction of force F that is a function of displacement x. The bilinear model as in Figure 7 makes the assumption of having only linear deformation [20][36]. At first, when the drill bit strikes the rock, the compressive force F linearly increases with the slope of the loading spring constant k_1 [20][22][36]. After the initial compression, the drill bit starts to experience extension where the force F decreases to zero with a slope of the unloading spring constant k_2 that corresponds to

$$k_2 = \frac{k_1}{\gamma}, \tag{30}$$

where γ is the unloading parameter [20][36]. The lower the unloading parameter in Equation (30), the higher the displacement is when force reaches zero in Figure 7. A study from Depouhon et al. [36] further describes and justifies the physics behind the linear rock model. In the study experimental data is compared with simulations using different rock models [36].

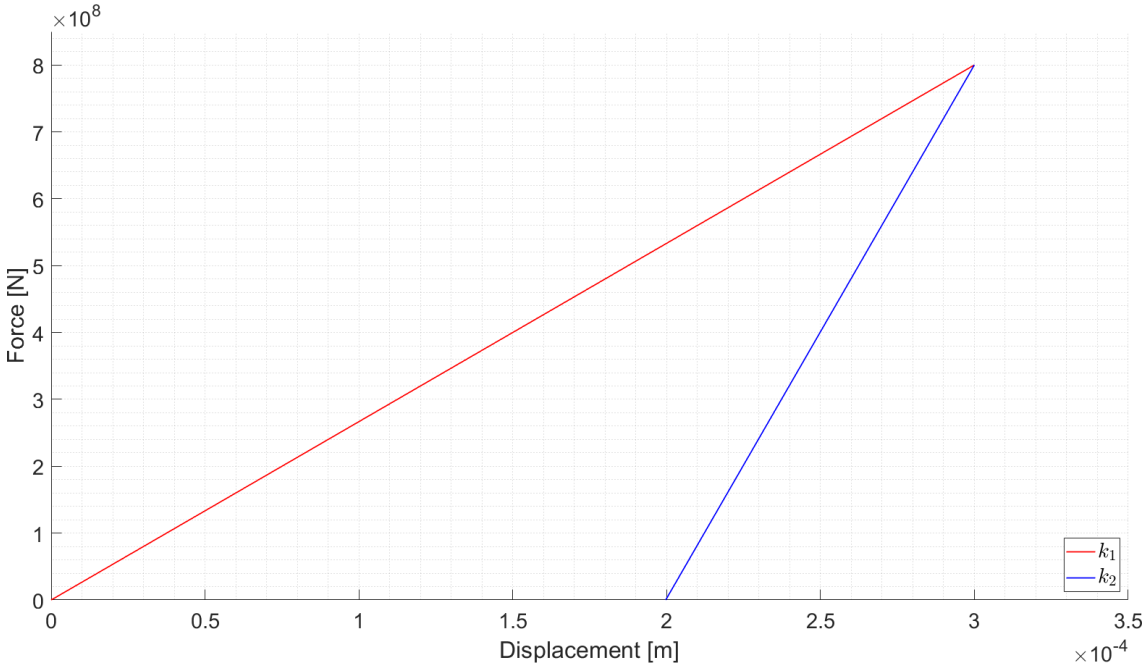

Figure 7. Bilinear stiffness model of bit-rock interface.[20][36]

Combining Equations (5) and (6) and solving change in length ΔL yields Equation (31)

$$\Delta L = \frac{FL}{EA}. \tag{31}$$

If the change in length ΔL can be considered as elastic displacement x in Hooke's law, then the stiffness k can be expressed by applying Equation (31) to Equation (1) as:

$$k = \frac{FEA}{FL} = \frac{EA}{L}, \tag{32}$$

where the axial stiffness k is a function of Young's modulus E, cross-sectional area A, and length L.

3.3 Measuring stress waves with strain gauges

To achieve high performance and efficiency in rock drilling, it is mandatory to understand how much energy from the percussion is transmitted to the rock and then reflected back to

the drill [23]. This can be done by measuring the first incident stress wave and comparing it to the first reflected stress wave. Analysing researching multiple reflections of the stress wave can give information about whether there are other issues in the process [11].

A common way to observe stress waves in drilling equipment is to measure the strain in an object by means of strain gauges [11][23]. Strain gauges are based on the relationship between electrical resistance R and the mechanical strain ε. The strain of an object can be calculated as:

$$\varepsilon = \frac{\Delta R}{R}\frac{1}{GF}, \tag{33}$$

where ΔR is change in electrical resistance, R is the reference resistance at zero strain, and GF is the gauge factor.[24][25] Typically the gauge factor GF has value of around two [11][24]. The changes in resistance ΔR can be marginal when comparing to the reference resistance R, thereby, an amplifier must be used [11].

Wheatstone bridges can be used to determine the unknown resistance within the circuit. Operation of Wheatstone bridge is based on the fact that the output voltage U_{out} is zero regardless of input voltage U_{in}.[11] A traditional Wheatstone bridge is shown in Figure 8a), where the bridge has four identical resistors.

As shown in Equation (33), if strain is applied to an electrical object, the object experiences a change in resistance — thereby, by replacing two of the resistors with strain gauges, we can create a bridge that works as the traditional Wheatstone bridge but is sensitive to strain. This circuit is shown in Figure 8b).[11]

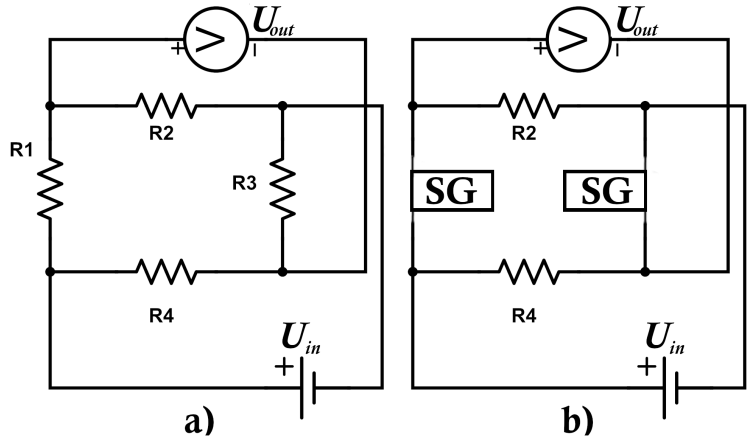

Figure 8. a) Wheatstone bridge [26] and b) modified bridge with strain gauges [11].

When the resistance of the strain gauges change, the voltage levels in the circuit start to differ and the output voltage U_{out} can be expressed as:

$$U_{out} = \frac{1}{4}\frac{\Delta R}{R}U_{in} = \frac{1}{4}GF\varepsilon U_{in}. \tag{34}$$

By measuring the output voltage from the circuit in Figure 8b), the only variable that is unknown in Equation (34) is the strain ε. After measuring the strain ε by the strain gauge, we can convert the strain to a stress σ by using Equation (4). To eliminate bending strain from the measurements, the circuit in Figure 8b) uses two strain gauges that are on opposite sides of the bridge. To calculate only the longitudinal strain from Equation (34),

$$U_{out} = \frac{1}{4}GF(\varepsilon_1 + \varepsilon_2)U_{in}, \tag{35}$$

in which both strain gauge sensors have their own strains ε_1 and ε_2.[11]

To measure the stress waves in case of rock drilling, the strain gauges are installed to an area of the drilling rod that is outside the borehole to avoid damaging the sensors [11]. While, the operation of a strain gauge is straightforward, its working principle is what works against itself when the temperature changes. When electrically conductive material experiences increase an in temperature, its resistance typically increases as well [27]. Since the drilling rods eventually heat up from the friction caused by the stress waves, the heat will conduct to the strain gauge, thereby changing its resistance.

3.4 Statistical methods

Statistical methods and analysis are used in thesis to mathematically interpret and compare the computed and measured data.

3.4.1 Correlation

The correlation coefficient C is used to express the strength of an association between two variables.[28] Equation (36) shows how the population correlation coefficient is calculated

$$C = \frac{cov(X,Y)}{\sqrt{Var(X)}\sqrt{Var(Y)}}, \tag{36}$$

where covariance $cov(X,Y) = \mathrm{E}(X-\mathrm{E}X)(Y-\mathrm{E}Y) = \mathrm{E}(XY)-\mathrm{E}X\mathrm{E}Y$ and $Var(X) = \mathrm{E}(X-\mathrm{E}X)^2$. Acknowledging these, Equation (36) can be rewritten as:

$$C(X,Y) = \frac{\mathrm{E}(X-\mathrm{E}X)(Y-\mathrm{E}Y)}{\sqrt{\mathrm{E}(X-\mathrm{E}X)^2}\sqrt{\mathrm{E}(Y-\mathrm{E}Y)^2}}. \tag{37}$$

When random variables X and Y are not correlated with each other, the correlation coefficient C equals to zero.[29] When calculating correlation coefficient C from Equation (37), its range of values is [-1,1], where -1 corresponds to perfect negative correlation. On the contrary, 1 corresponds to perfect positive correlation.[28] With perfect correlations, the information from one variable could be transferred to the correlated variable without a loss of information. In this thesis when the correlation is calculated within the incident stress wave, it is noted as C_i. Similarly, the reflected wave's correlation is noted as C_r.

3.4.2 Root Mean Square Error (RMSE)

The Root Mean Square Error ($RMSE$) is a common way to identify the error between observed and predicted data. $RMSE$ is calculated as:

$$RMSE = \sqrt{\left(\sum_{i=1}^{n}(x_i - \hat{x}_i)^2\right)/n}, \tag{38}$$

where x_i are observed values, $\hat{x}_i$ predicted values, and n is the number of samples.[30] Because in Equation (38) the mean squared error is square rooted, $RMSE$ has the same unit as its input variable x. RMSE of the incident wave is noted as $RMSE_i$ and similarly, the reflected wave as $RMSE_r$.

3.4.3 Sensitivity analysis

A sensitivity analysis is a mathematical method that is used to investigate variation in the output of a numerical model when the model's input variables experience known variation. With the help of a sensitivity analysis, uncertainties in the output can be distributed into different sources by applying minimal changes to the model's input variables.[31] In this thesis, a sensitivity analysis is used to visualize the effect of changing physical constants such as speed of sound or spring constants of the rock model. Since this thesis' research problem concerns continuous data and not discrete one, sensitivity analysis is conducted by overlaying numerical models next to each other and comparing their performance to the measurement mean in terms of correlation and root mean square error. In addition to analysing changes in the input variables, variances in the measurements can be visualized performing a shade plot which overlays all individual percussions from the drill into a single figure.

3.5 Stress analysis with the Finite Element Method (FEM)

The Finite Element Method (FEM) is a numerical method which original use case is to solve problems of stress analysis. Nowadays it has been applied in numerous of other problems such as fluid flow analysis and thermal analysis. In a case of stress analysis, the problem roots into solving Hooke's equation — that being, determining material displacements when material experiences external forces. For modeling any object, FEM takes an approach of distributing the problem into finite number of elements that are made of nodes and then the elements can interact with neighbouring elements. The formation that these elements create is called the mesh.[12] When taking an approach of considering these individual nodes as atoms, the mesh can be thought of being an extensive Lorentez

oscillator model of mechanical mass–and–spring system.

One of the first tasks in conducting Finite Element Analysis (FEA) is to define the geometry of the system. Nowadays designing the system is commonly done by using various of Computer Aided Design (CAD) software that come with graphical user interfaces that can be used to design complex objects.[12] This Master's Thesis takes advantage of using existing designs that are used to manufacture rock drilling parts. With the help of accurate design geometry, it is possible to reduce the error between a numerical model and measurement.

Once the system geometry is defined, meshing is done. Since the whole problem domain is divided into elements by using a set of nodes, the solution across the elements can be approximated by using linear or polynomial functions.[12] When meshing, it is important to understand the complexity of the mesh. Having higher density of elements and thereby higher number of nodes, the complexity of the mesh increases. On the other hand, with more dense mesh, approximations between elements have smaller error due to shorter distance used in approximation.

For defining an appropriate mesh, the element type and shape must be selected with care. If the geometry does not require higher dimension than 1D, the elements are expressed as lines. Whereas, having 2D space requires more complex mesh which is usually made from triangular or quadrilateral elements. While quadrilateral elements can provide more accurate approximations than triangular elements, generating mesh made from quadrilateral elements can be challenging. Going from 2D to 3D space, the model can fundamentally be used for all 3D solids by using tetrahedron or hexahedron shapes.[12] From the aspect of computation time, a conversion from triangle to tetrahedron is more efficient than going from quadrilateral element to hexahedral.

Besides of having defined geometry for the mesh, the physical properties of the elements need to be configured in a way that they correspond to material properties of bodies. To conduct stress analysis, it is essential to determine Young's modulus and shear modulus for a specified area of the mesh. Commonly, material properties are obtained by conducting own experiments or by utilizing literature.[12] This Master's Thesis uses experimental material properties that are based on literature.

3.5.1 Key equations used in FEM

The FEM equation for expressing how external forces affect an individual element's node in its local coordinate system is

$$\mathbf{f}_e = \mathbf{k}_e\mathbf{d}_e + \mathbf{m}_e\ddot{\mathbf{d}}_e, \tag{39}$$

where $\mathbf{f}_e$ is the force vector of the total forces taking place in a node, while $\mathbf{k}_e$ and $\mathbf{m}_e$ are the stiffness and mass matrices that are respectively multiplied by displacement vector $\mathbf{d}_e$ and acceleration $\ddot{\mathbf{d}}_e$.[12] Equation (39) hereby expresses node as a mass–spring–system that obeys Hooke's law and Newton's second law.

By conducting coordinate transformation with transformation matrix $\mathbf{T}$, Equation (39) can be expressed on the global coordinate system. Coordinate transformation of Equation (39) is

$$\mathbf{F}_e = \mathbf{K}_e\mathbf{D}_e + \mathbf{M}_e\ddot{\mathbf{D}}_e, \tag{40}$$

where $\mathbf{F}_e$, $\mathbf{K}_e$, $\mathbf{D}_e$, $\mathbf{M}_e$, and $\ddot{\mathbf{D}}_e$ in Equation (40) are in the global coordinate system.[12]

The benefit of having a matrix representation of nodal FE Equation (40) is that the forces from neighbouring elements can be assembled together to form the global FE equation system:

$$\mathbf{F} = \mathbf{K}\mathbf{D} + \mathbf{M}\ddot{\mathbf{D}}. \tag{41}$$

With the help of Equation (41), displacements at any node in the problem domain can be expressed. To make Equation (41) applicable for transient excitation, that is a highly dynamic and time-dependent force experienced on the structure, Equation (42) is used

$$\mathbf{F} = \mathbf{K}\mathbf{D} + \mathbf{C}\dot{\mathbf{D}} + \mathbf{M}\ddot{\mathbf{D}}, \tag{42}$$

where

$$\mathbf{K} = \sum_{e} \int_{V_e} \mathbf{B}^{\mathrm{T}} \mathbf{E} \mathbf{B} dV, \tag{43}$$

$$\mathbf{C} = \sum_{e} \int_{V_e} c_e \mathbf{N}^{\mathrm{T}} \mathbf{N} dV, \tag{44}$$

and

$$\mathbf{M} = \sum_{e} \int_{V_e} \rho \mathbf{N}^{\mathrm{T}} \mathbf{N} dV. \tag{45}$$

The stiffness matrix **K** in Equation (43) consists of the strain matrix **B** and Young's modulus matrix **E**. The damping coefficient matrix **C** in Equation (44) and the mass matrix **M** in Equation (45) both have shape function matrices **N** that determine the way of interpolation. In Equation (44) c_e is the damping coefficient which is determined from experimental data.[12]

The classical way of solving Equation (42) is to use a central difference algorithm that is based on a residual method. The residual force vector $\mathbf{F}^{residual}$ is expressed as:

$$\mathbf{F}^{residual} = \mathbf{F} - \mathbf{F}^{int} = \mathbf{F} - [\mathbf{C}\dot{\mathbf{D}} + \mathbf{K}\mathbf{D}] = \mathbf{M}\ddot{\mathbf{D}}, \tag{46}$$

where the internal force $\mathbf{F}^{int}$ at time t is

$$\mathbf{F}^{int} = [\mathbf{C}\dot{\mathbf{D}} + \mathbf{K}\mathbf{D}], \tag{47}$$

and the acceleration vector $\ddot{\mathbf{D}}$ can be solved to

$$\ddot{\mathbf{D}} = \mathbf{M}^{-1}\mathbf{F}^{residual}. \tag{48}$$

In a central difference algorithm there are three fundamental equations to express element's movement in the problem domain. Equation (49) is used to approximate node

displacement after time step Δt by using current and previous displacement. Similarly, Equation (50) approximates node velocity by relating current acceleration and previous velocity. To solve acceleration at time t from Equation (51), displacements at times $t \pm \Delta t$ and t are used.[12]

$$\mathbf{D}_{t+\Delta t} = 2\Delta t\dot{\mathbf{D}} + \mathbf{D}_{t-\Delta t} \tag{49}$$

$$\dot{\mathbf{D}}_{t+\Delta t} = 2\Delta t\ddot{\mathbf{D}} + \dot{\mathbf{D}}_{t-\Delta t} \tag{50}$$

$$\ddot{\mathbf{D}}_t = \frac{1}{(\Delta t)^2}(\mathbf{D}_{t+\Delta t} - 2\mathbf{D}_t + \mathbf{D}_{t-\Delta t}) \tag{51}$$

With Equations (49) and (51), the displacement at time $t - \Delta t$ can be solved into

$$\mathbf{D}_{t-\Delta t} = \mathbf{D}_t - \Delta t\dot{\mathbf{D}} + \frac{(\Delta t)^2}{2}\ddot{\mathbf{D}}_t. \tag{52}$$

By acknowledging the initial conditions from where the system starts to operate, Equations (48) and (52) can be used to approximate how external forces affect the node displacement.

In the case of one-dimensional problem domain, the element's strain in the global coordinate system ε can be written in form of a strain matrix $\mathbf{B}$, a transform matrix $\mathbf{T}$ and the element displacement $\mathbf{D}_e$, as $\varepsilon = \mathbf{BTD}_e$. Since $\sigma = E\varepsilon$, the stress along x-axis σ_x is

$$\sigma_x = E\varepsilon = E\mathbf{BTD}_e. \tag{53}$$

With the help of Equation (52), dynamical stress changes can be solved with Equation (53).[12]

4 MATERIAL AND SOFTWARE

This section of the thesis shows how stress wave measurements are conducted with commonly used strain gauges. For comparison, different software are used to study the possibility to numerically compute similar data as in the measurements. For visualizing, processing, and analysing the signals received from the measurement device and numerical models, MATLAB R2022a is used. MATLAB by Mathworks is programming and numeric computing platform that can be used for iterative analyses and design processes [32].

4.1 Measurement equipment

In this thesis, two different drilling systems for stresses are utilized. Both systems use the same rock drill but different tools are listed in Table 1.

Table 1. Differences between A and B threaded systems.

	A	**B**
Proportional rod cross-sectional area	1:1	4:3
Strain gauge rod length [ft]	12	14
Proportional drill bit diameter	1:1	5:4

4.1.1 Drilling rods with strain gauges

Strain gauges are used in this thesis to measure the stress waves of drilling rods. The way these strain gauges are electrically connected is illustrated in Figure 8b). Strain gauges rely on a conductor's change in resistance which is caused by strain. For further theoretical operation of strain gauges, please refer to Section 3.3.

Figure 9 shows three drilling rods that have strain gauges installed to them. The position of the strain gauges is chosen to provide a good quality signal while also ensuring an adequate endurance of the sensor. Placing the strain gauge close to the shank could cause an increase of noise in the signal due to the higher temperatures and vibrations from the drill. On the other hand, if the sensor is closer to the drill bit, the cabling would tangle up inside the borehole and could thereby get damaged. Therefore, the strain gauge and its

cabling are installed in the middle of the first drilling rod that is above the surface [11]. One of the biggest challenges in measuring with strain gauges is to keep the vibrations caused by the drilling equipment as low as possible to avoid breaking the delicate strain gauge sensors [11]. The cables seen in Figure 9 are used to transmit the voltage signal from the Wheatstone's bridge to a computer for data logging and processing.

Figure 9. Strain gauge rods with strain gauges installed.

After the voltage change in the bridge has been converted to stress σ, the signal can be used to analyse propagating stress waves in the drilling rods. Figure 10 shows how the stress σ changes as a function of time after a single piston strike. Similarly, Figure 11 has a short sample of stress wave where different stresses are classified as follows: incident stress σ_i, reflected stress from drill bit $\sigma_{r,b}$, reflected tensile stress $\sigma_{r,t}$, and reflected compressive stress $\sigma_{r,c}$.

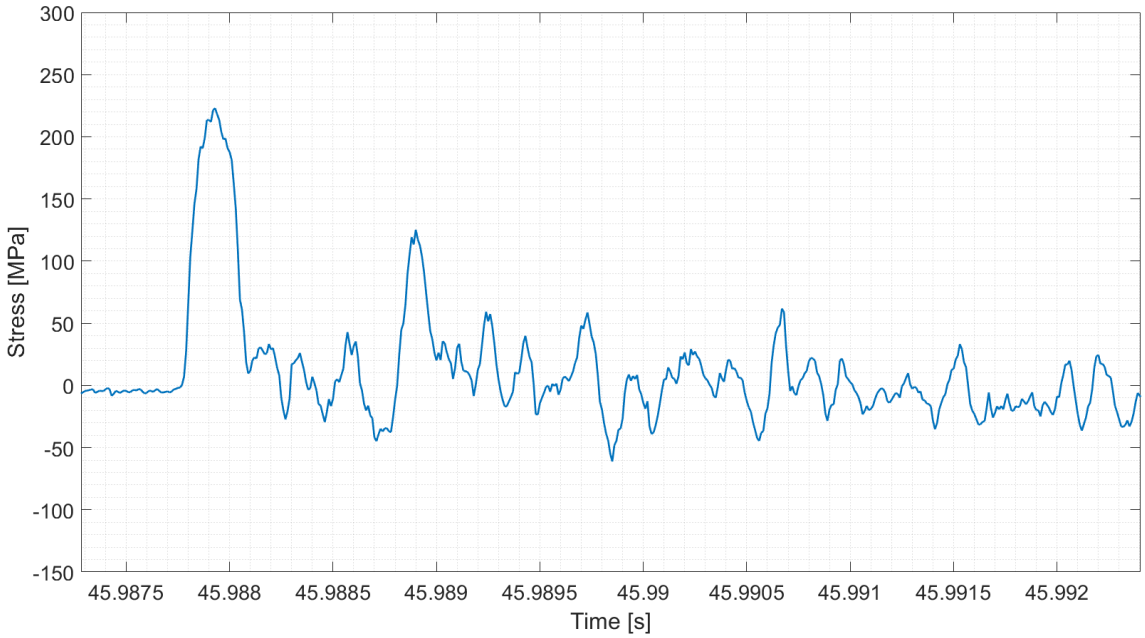

Figure 10. Stress wave propagating through a drilling rod.

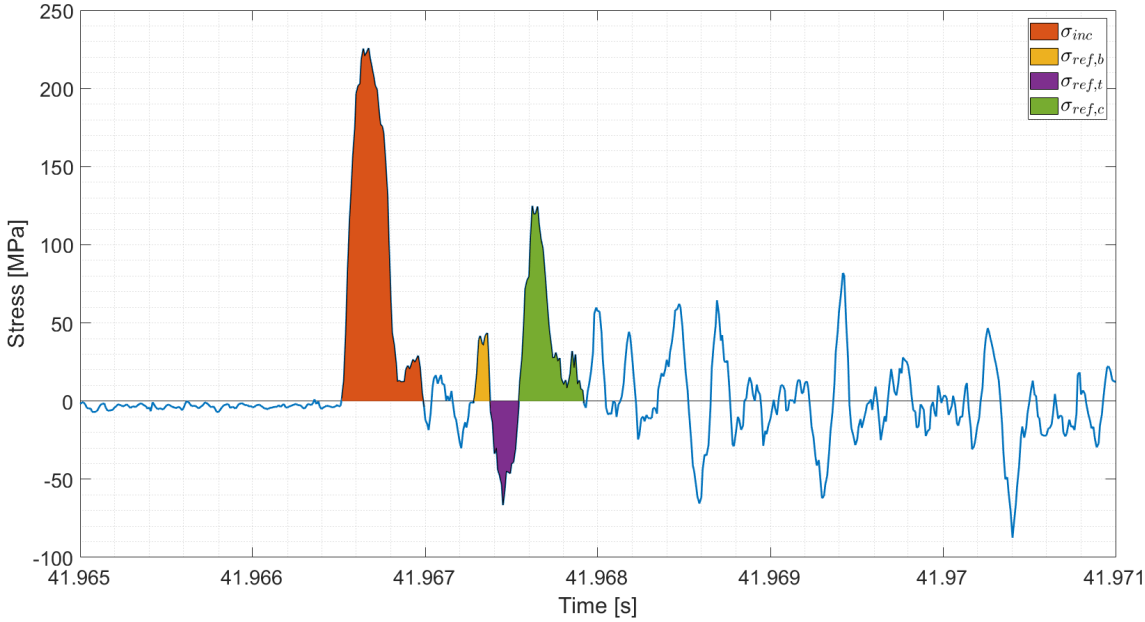

Figure 11. Classified stresses from a single piston stroke.

4.2 Numerical models of stress waves

This thesis uses numerical drilling process models to computationally create as similar as possible stress data that can be observed with strain gauge measurements. When creating numerical models, it is compulsory to make problem domains that correspond to the one used when measuring with strain gauges. Having different geometries and cross-sectional areas will lead to incorrect values in stress, as the stress σ is proportional to area A as presented in Equation (6).

When creating numerical models that represent a physical phenomenon, it is mandatory to be aware what physical properties need to be set and what are the values for those. In this thesis, the physical properties are not separately measured but values from other extensive researches are used. Tables 2 and 3 show the physical constants that are used in this research unless stated differently.

Table 2. Physical properties of steel.[22][33][34][35]

Young's modulus E	210 [GPa]
Density of steel ρ	7800 [kg/m^3]
Poisson ratio ν	0.3

Table 3. Bilinear rock model's parameters.

Loading spring constant k_1	$800 \cdot 10^6$ N/m
Unloading spring constant k_2	$800 \cdot 10^7$ N/m
Unloading parameter γ	0.1

4.2.1 Software A and Software B

Software A is one of the software that is used to create numerical models for the thesis. Software A is a commercial software that is based on finite element method (FEM). Software A includes a multi-physics solver that allows to solve computational fluid dynamics and structural changes. In this thesis, Software A is used to create FEM models where the force and thereby stress propagates from the piston/shank percussion towards the drill bit from which it reflects back towards the drill.

The second software used to create numerical models is Software B. Software B is similar to Software A as they share a similar way to numerically compute stresses in systems based on FEM. Both Software A and Software B models are structurally similar to each other where there are own parts for piston, shank, drilling rods, bit, and rock. Each part in the system have their own unique physical properties, such as, density, Young's modulus, and elastic constant. In each FEM system, shank, drilling rods and bit are designed as they are made for the real drill rigs.

One of the downsides of models created with Software A and Software B is that there is no complete rock drill, and the piston is thought to be a floating object that strikes the shank with specified velocity. In addition to missing rest of the rock drill, the system does not experience gravitational forces that affect stresses, especially when drilling vertically.

Both Software A and Software B have a high density of elements in the mesh, with the shortest distance between elements being 1.5 mm at the threads where the geometry is the most detailed. The mesh itself is assembled in the 2D-axisymmetric space. The downside of having an axisymmetric problem domain is that the threads will not have helical structure.

5 RESULTS

5.1 Measurements using thread type A

Figure 12 shows the stress σ in function of time from one drilling measurement session with a system using thread type A. At the beginning and at the end of the signal, there is no contact between the drill bit and the rock. The drill bit starts to collide with the rock 15 seconds after the beginning of the recording. The measurement session is conducted by gradually increasing the percussion pressure as in Figure 13. This leads to increasing feed pressure in Figure 14. By increasing percussion and feed pressure, the piston of the rock drill experiences higher forces and accelerations, thereby making the impact velocity higher which leads to higher stresses and energies.

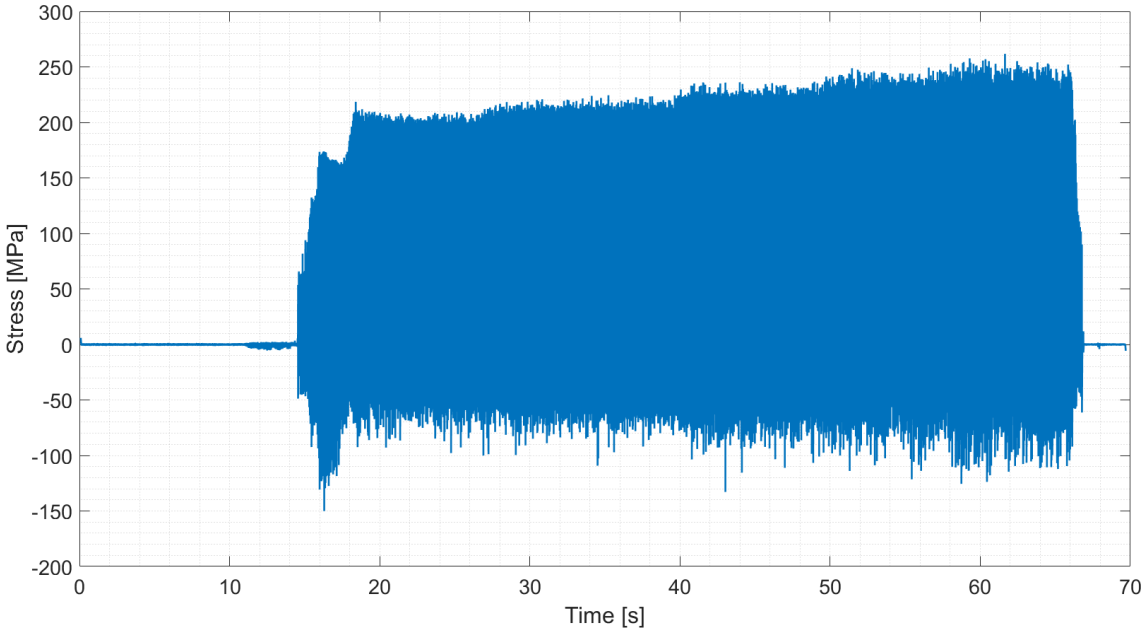

Figure 12. Strain gauge measurement from one drilling session.

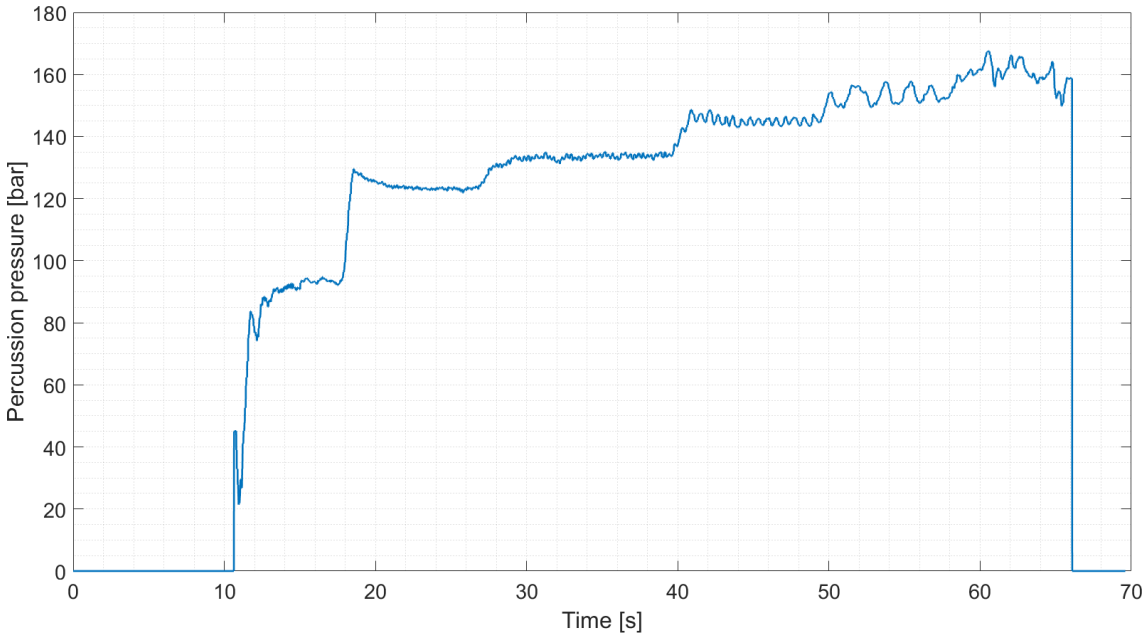

Figure 13. Percussion pressure measurement from one drilling session.

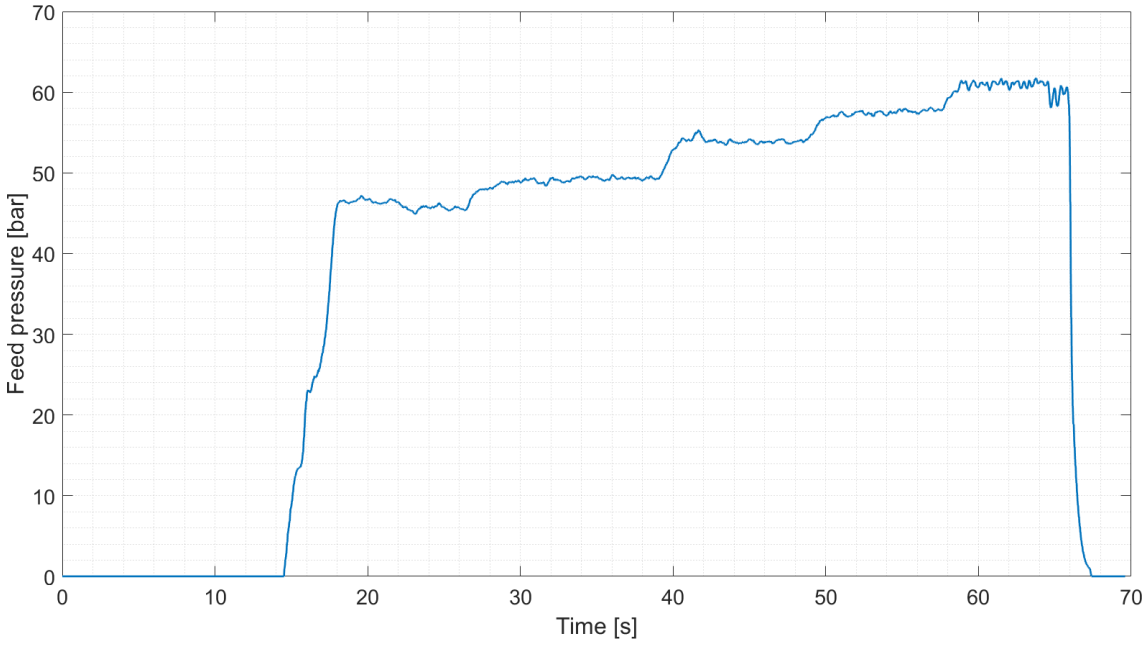

Figure 14. Feed pressure measurement from one drilling session.

Due to changes in percussion and feed pressure, the data in Figure 12 is classified into five different intervals according to the percussion pressures seen in Figure 13. These intervals

are respectively 120 bar, 130 bar, 140 bar, 150 bar, and 160 bar. After dividing the whole measurement data into shorter sections, the stress waves can be examined with respect to percussion pressure, as shown in Figures 15 and 16, where the black graph corresponds to interval's mean strike. Red vertical lines are used to annotate where incident and reflected waves start and end.

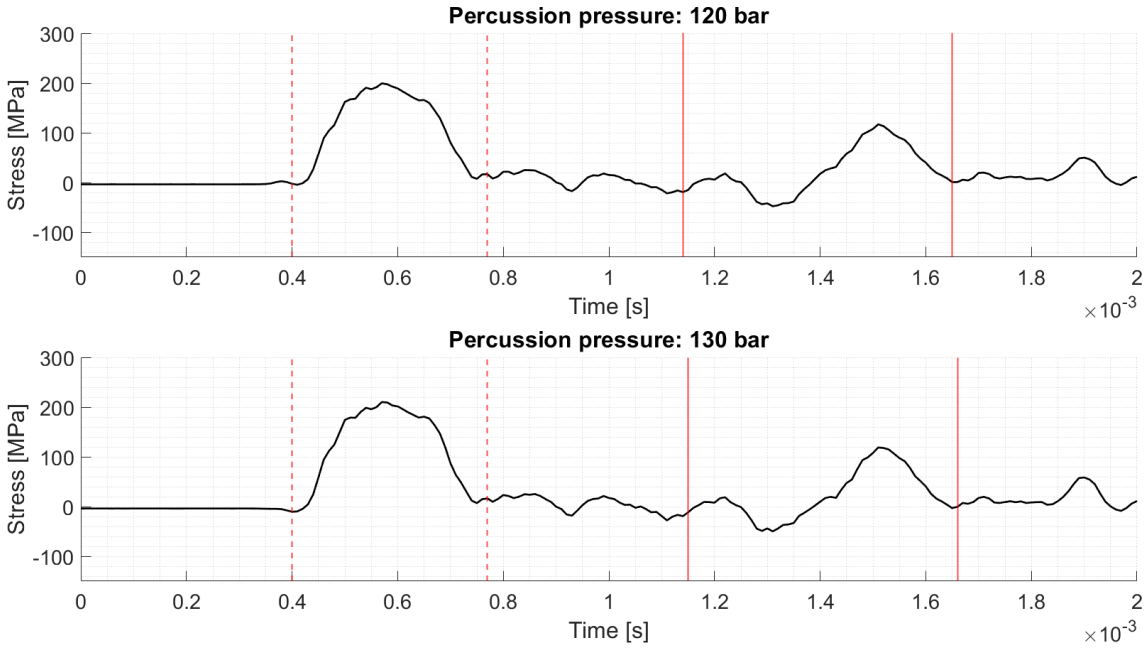

Figure 15. Mean stress waves of A threaded system with 120 bar and 130 bar percussion pressure.

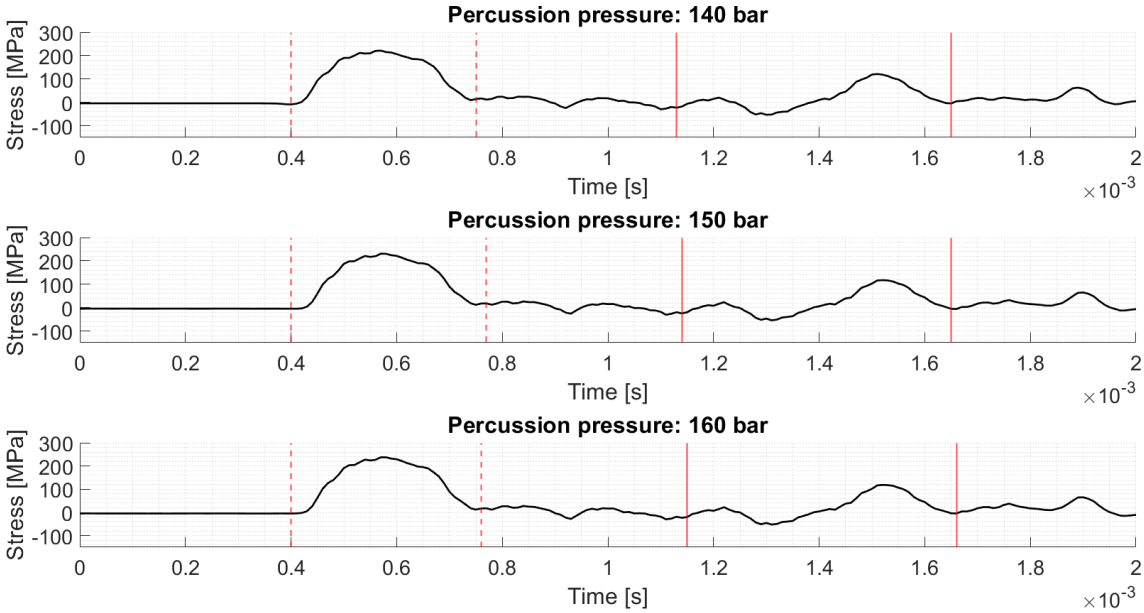

Figure 16. Mean stress waves of A threaded system with 140 bar, 150 bar, and 160 bar percussion pressure.

Table 4 compares the maximum compressive stresses in the incident wave σ_i and reflected wave $\sigma_{r,c}$ for the different percussion pressure levels. In addition to these, the greatest tensile stress during the reflected wave $\sigma_{r,t}$ is included. As shown in Table 4, stresses in the incident wave increase as the percussion pressure increases. Despite of the increasing stresses in the incident wave, stresses in the reflected wave do not directly correlate with the percussion pressure.

Table 4. Thread type A measurements' mean stress amplitudes with respect to percussion pressure.

p_p [bar]	max(σ_i) [MPa]	min($\sigma_{r,t}$) [MPa]	max($\sigma_{r,c}$) [MPa]
120	199.38	-47.76	116.96
130	210.09	-49.85	118.77
140	221.40	-52.95	121.33
150	230.92	-54.38	117.67
160	237.66	-52.36	118.58

Similarly to Table 4, Table 5 compares the mean energies with respect to the percussion pressure. In Table 5, $E_{\sigma,i}$ is the incident wave energy from the mean strike — similarly,

$E_{\sigma,r}$ is the reflected wave's energy. As the reflected wave's energy $E_{\sigma,r}$ is nearly constant, even though the incident wave energy increases, the efficiency η shows a slight increase.

Table 5. Thread type A measurements' mean energies with respect to percussion pressure.

p_p [bar]	$E_{\sigma,i}$ [J]	$E_{\sigma,r}$ [J]	η
120	290.49	62.25	0.786
130	331.91	62.74	0.811
140	364.96	65.41	0.821
150	390.61	62.65	0.840
160	413.83	63.09	0.848

5.2 Measurements using thread type B

For comparing the effect of having different thread geometries, bit sizes, and rod lengths, another set of measurements and simulations are conducted. The following measurements use the same rock drill as the previously used A threaded system but with exceptions shown in Table 1. Figures 17 and 18 present mean stress waves of B threaded system's simulations with percussion pressures of 140 bar, 160 bar, 180 bar, and 200 bar.

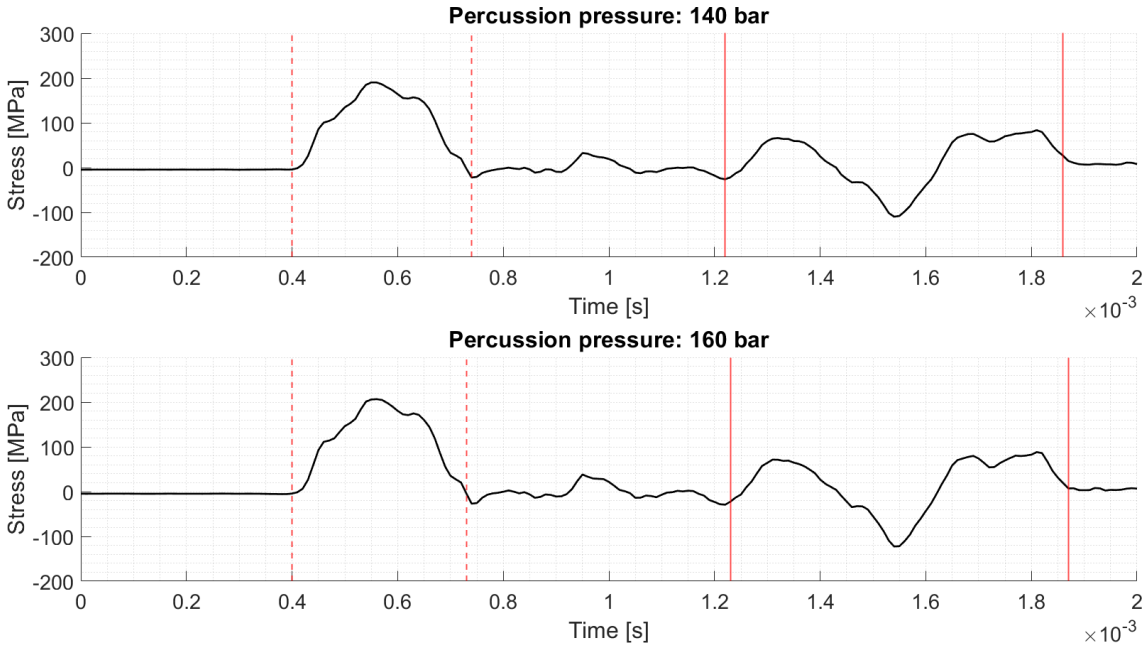

Figure 17. B threaded system mean stress waves with 140 bar and 160 percussion pressure.

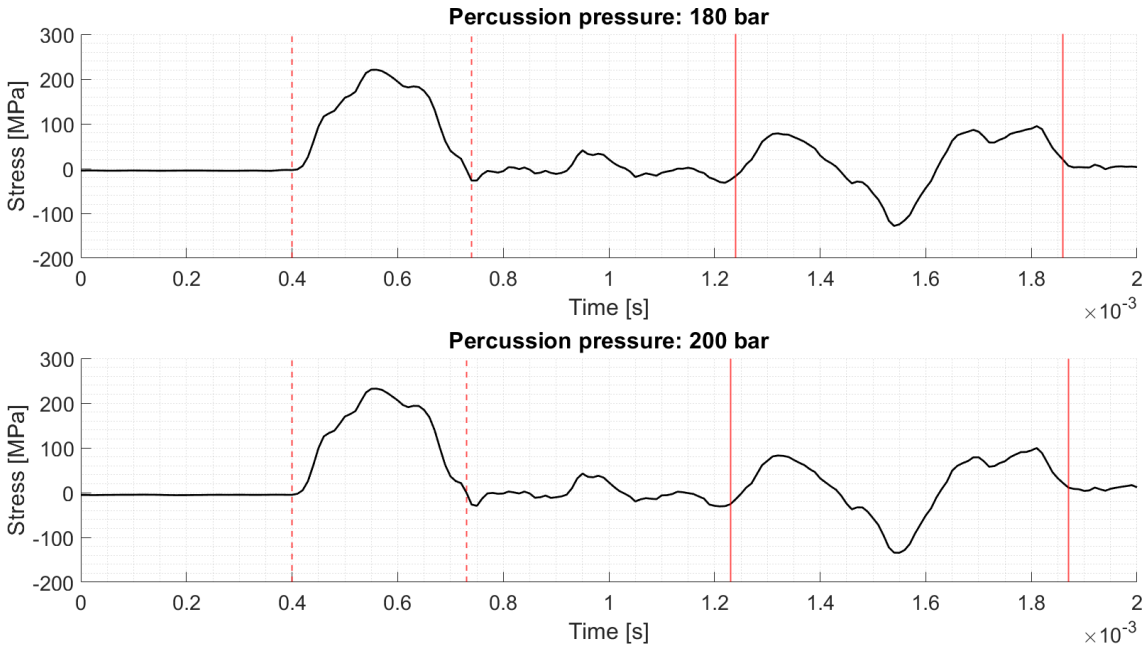

Figure 18. B threaded system mean stress waves with 180 bar and 200 percussion pressure.

Table 6 lists the maximum compressive stresses in the incident wave σ_i and reflected wave's highest tensile stress $\sigma_{r,t}$ and compressive stress $\sigma_{r,c}$ for each measurement with thread type B.

Table 6. Thread type B measurements' mean stress amplitudes with respect to percussion pressure.

p_p [bar]	max(σ_i) [MPa]	min($\sigma_{r,t}$) [MPa]	max($\sigma_{r,c}$) [MPa]
140	190.25	-109.63	83.59
160	206.54	-122.43	88.40
180	220.75	-128.15	94.90
200	232.26	-134.35	99.64

Table 7 presents incident $E_{\sigma,i}$ and reflected wave energies $E_{\sigma,r}$ in joules for each percussion pressure's mean stress wave. In addition to energies, stress wave efficiency η is shown.

Table 7. Thread type B measurements' mean energies with respect to percussion pressure.

p_p [bar]	$E_{\sigma,i}$ [J]	$E_{\sigma,r}$ [J]	η
140	322.27	109.17	0.661
160	386.41	122.49	0.683
180	440.88	133.22	0.698
200	493.07	141.45	0.713

Figure 19 shows a comparison between A and B threaded measurements at 140 bar percussion pressure. Since the B threaded measurements use a two feet longer strain gauge drilling rod, the reflection does not occur at the same time as for the A threaded measurement. Despite of non-matching stress wave reflections, the B threaded mean measurement experiences a twice as high tensile stress compared with thread type A.

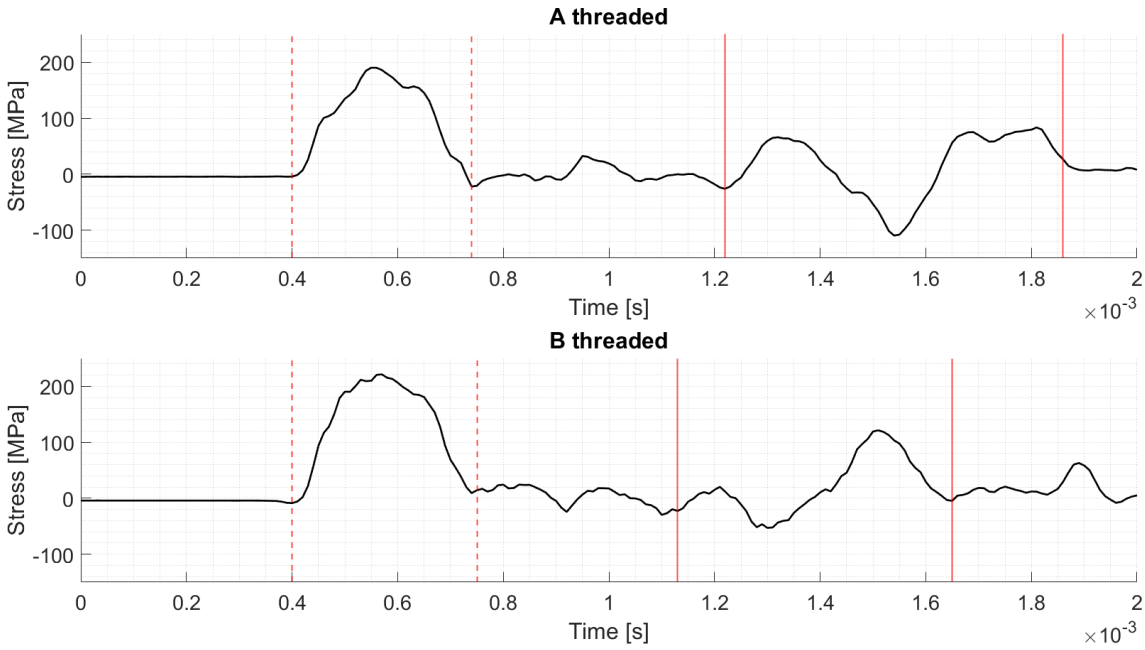

Figure 19. Thread type A and B measurement mean stress waves at 140 bar percussion pressure.

5.3 Numeric simulation model of system with A thread

For creating the first numerical simulations of A threaded system, Software A and Software B is used. Both simulations use the same accurate models of shank, drilling rod, and

drill bit. In Figures 20 and 21 numerical simulations are being overlayed on top of measurement data from Figures 15 and 16. Even though the incident waves are in-phase with the measurement means, for all percussion levels the reflected stress wave is out-of-phase in Figures 20 and 21.

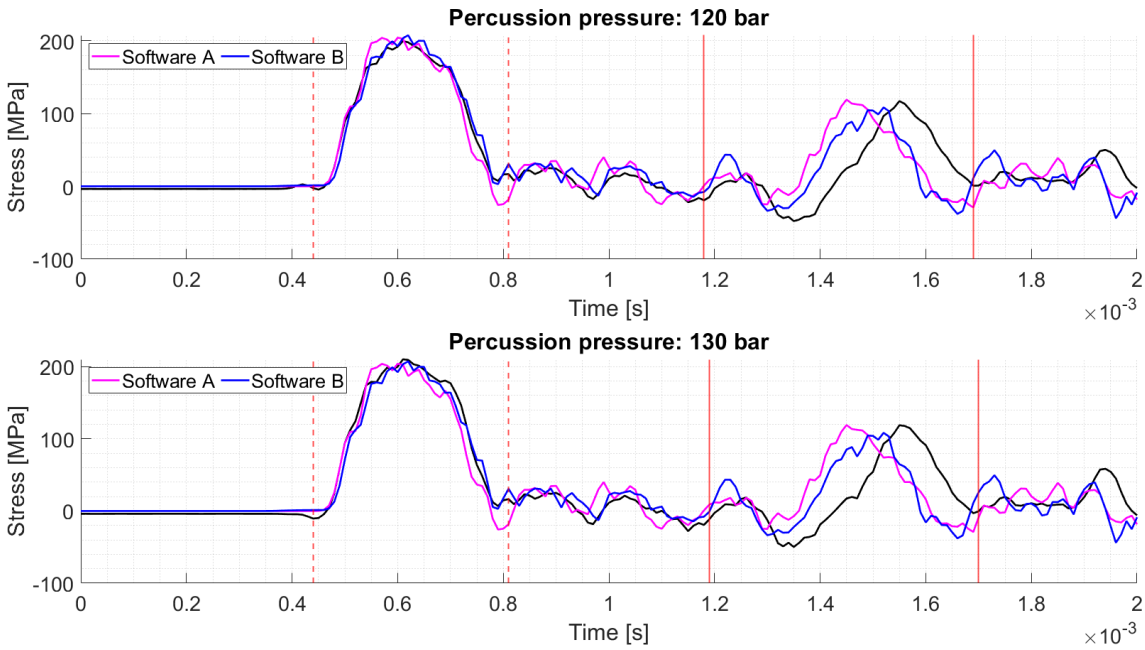

Figure 20. Thread type A stress wave simulations with Software A and Software B at 120 bar and 130 bar percussion pressure.

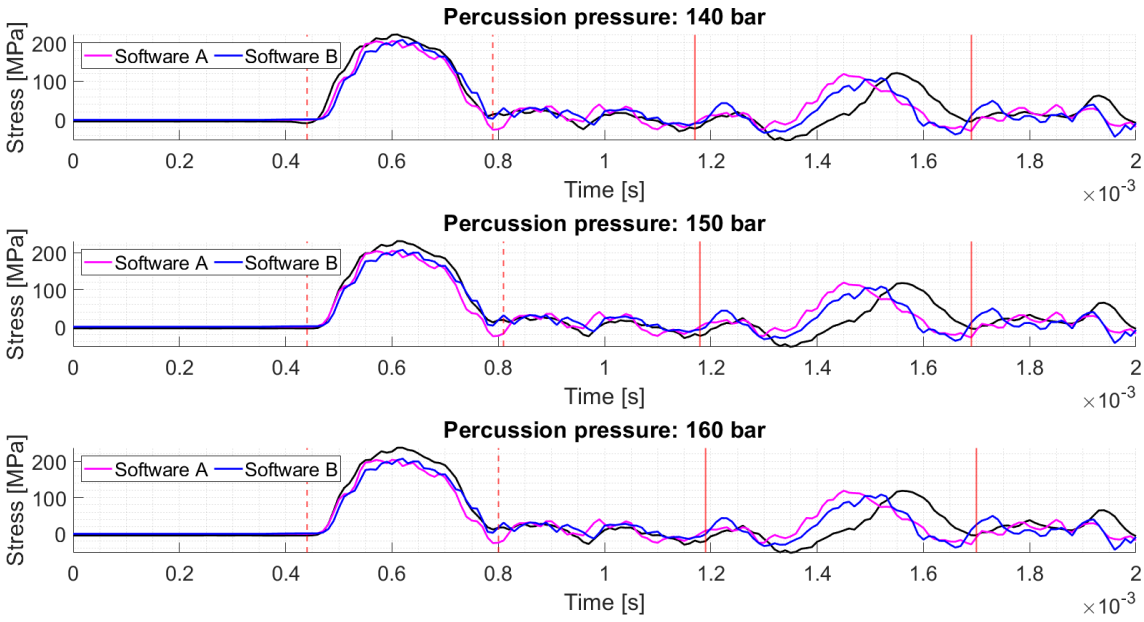

Figure 21. Thread type A stress wave simulations with Software A and Software B at 140 bar, 150 bar, and 160 bar percussion pressure.

Tables 8 and 9 asses the simulation performances in form of root mean square error and correlation with the respect to measurement mean at different percussion pressures. $RMSE$s are calculated separately for the incident wave and the reflected wave — error of these are denoted as $RMSE_i$ and $RMSE_r$, respectively. The same approach is used in Table 9 for correlations C_i and C_r.

Table 8. Software A and Software B incident and reflection wave errors of A threaded system at different percussion pressures.

	Software A		**Software B**	
p_p [bar]	$RMSE_i$ [MPa]	$RMSE_r$ [MPa]	$RMSE_i$ [MPa]	$RMSE_r$ [MPa]
120	15.88	59.60	10.07	49.25
130	19.22	62.63	12.55	52.30
140	19.88	60.58	25.17	49.49
150	25.70	65.31	21.00	55.34
160	28.77	66.29	25.53	56.49

Table 9. Software A and Software B incident and reflection wave correlations of A threaded system at different percussion pressures.

	Software A		**Software B**	
p_p [bar]	C_i	C_r	C_i	C_r
120	0.984	0.296	0.992	0.525
130	0.979	0.254	0.990	0.474
140	0.988	0.315	0.962	0.540
150	0.984	0.198	0.992	0.421
160	0.985	0.187	0.991	0.400

5.3.1 Differentiating rock model

Figures 22 and 23 present six different Software A simulations where k_1 value changes. The simulations are run with k_1 values of 250 MN/m, 350 MN/m, 450 MN/m, 550 MN/m, 650 MN/m, and 800 MN/m. For all percussion pressure levels, with increasing k_1 values the tensile stresses are lower. On the other hand, the compressive stress starts earlier with higher k_1.

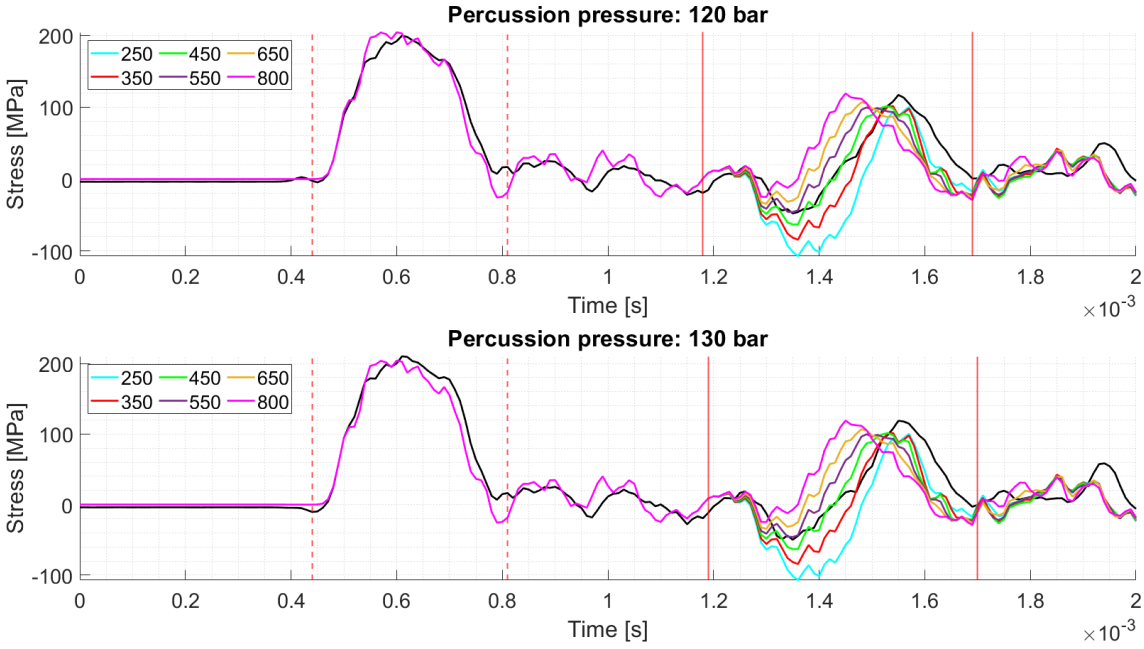

Figure 22. Software A stress wave simulations with differentiating k_1 at 120 bar and 130 bar percussion pressures.

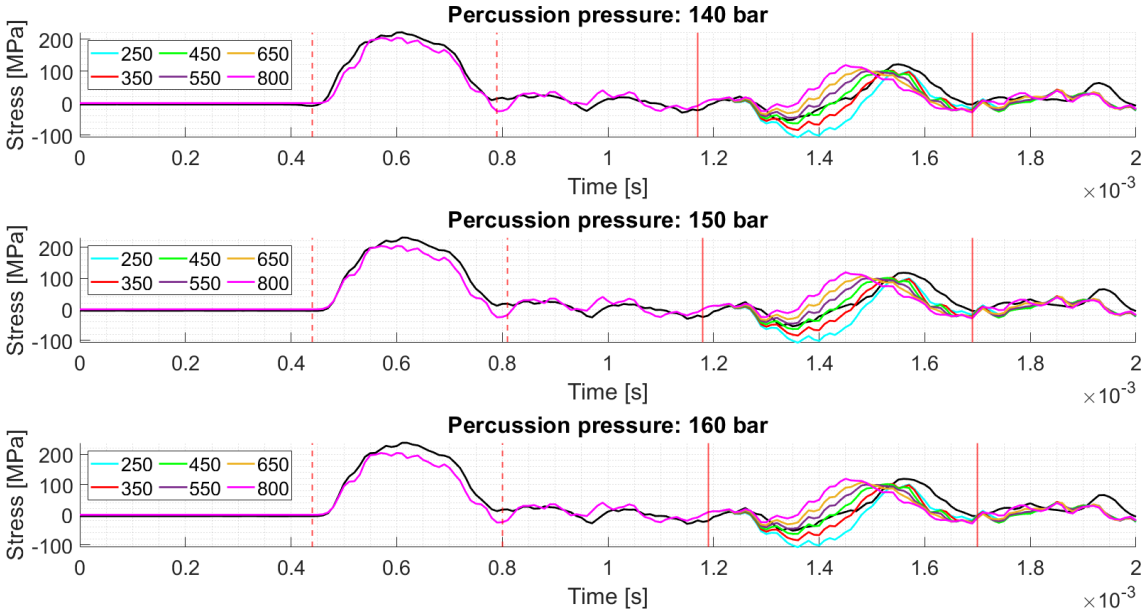

Figure 23. Software A stress wave simulations with differentiating k_1 at 140 bar, 150 bar, and 160 bar percussion pressures.

Figure 24 presents a view that magnifies on the area where the reflected stress wave starts in Figure 22. From Figure 24, it can be seen how the simulation signals start to deviate from each other when k_1 is different. If the beginning of the deviation is where the reflection starts, then the annotated vertical red line is off by 10 μs.

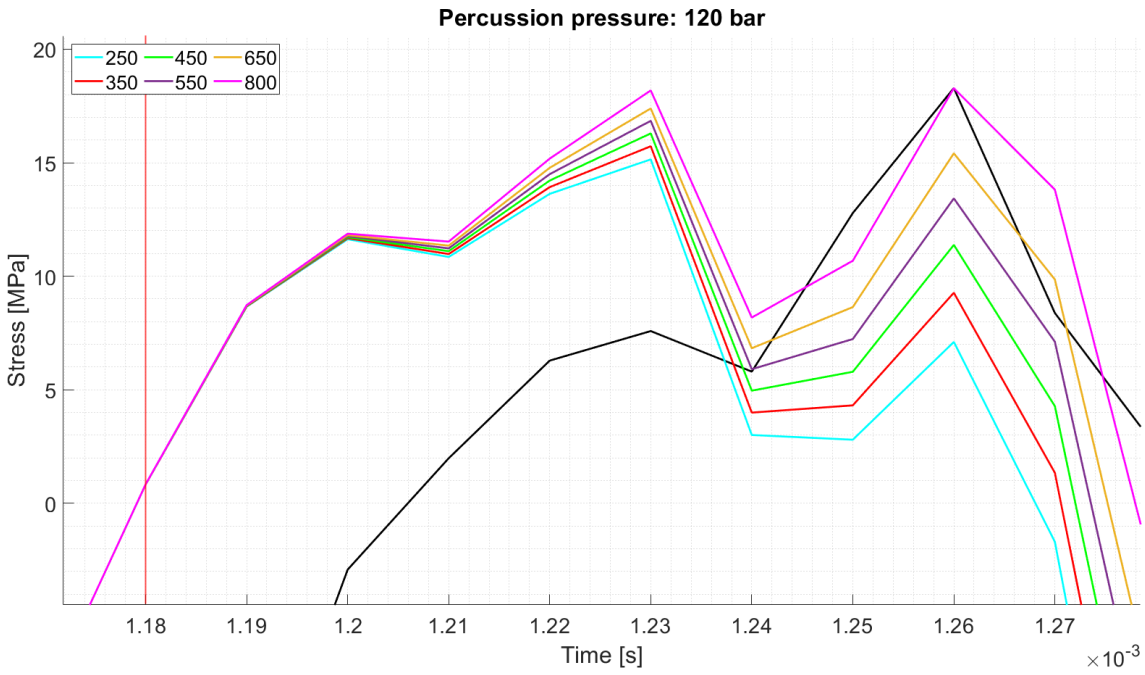

Figure 24. Signal deviation from differentiating k_1 with Software A.

Table 10 shows the errors between the simulations with different k_1 values and the measurement average at a percussion pressure 120 bar.

Table 10. Software A simulations' errors with differentiating k_1 at 120 bar p_p.

k_1 [MN/m]	$RMSE_i$ [MPa]	$RMSE_r$ [MPa]
250	15.88	47.64
350	15.88	31.43
450	15.88	28.08
550	15.88	35.01
650	15.88	44.94
800	15.88	59.61

Similarly to Table 10, Table 11 presents the incident wave and reflected wave correlations C_i and C_r for models from Software A.

Table 11. Software A simulations' correlations with differentiating k_1 at 120 bar p_p.

k_1 [MN/m]	C_i	C_r
250	0.984	0.953
350	0.984	0.960
450	0.984	0.895
550	0.984	0.767
650	0.984	0.590
800	0.984	0.296

Figures 25 and 26 show simulation results obtained with Software A where the unloading parameter γ is 0.05, 0.1 and 0.15. From the simulations it can be seen that by varying γ, it is possible to achieve higher compressive stress in the reflected wave without affecting the signal prior to it.

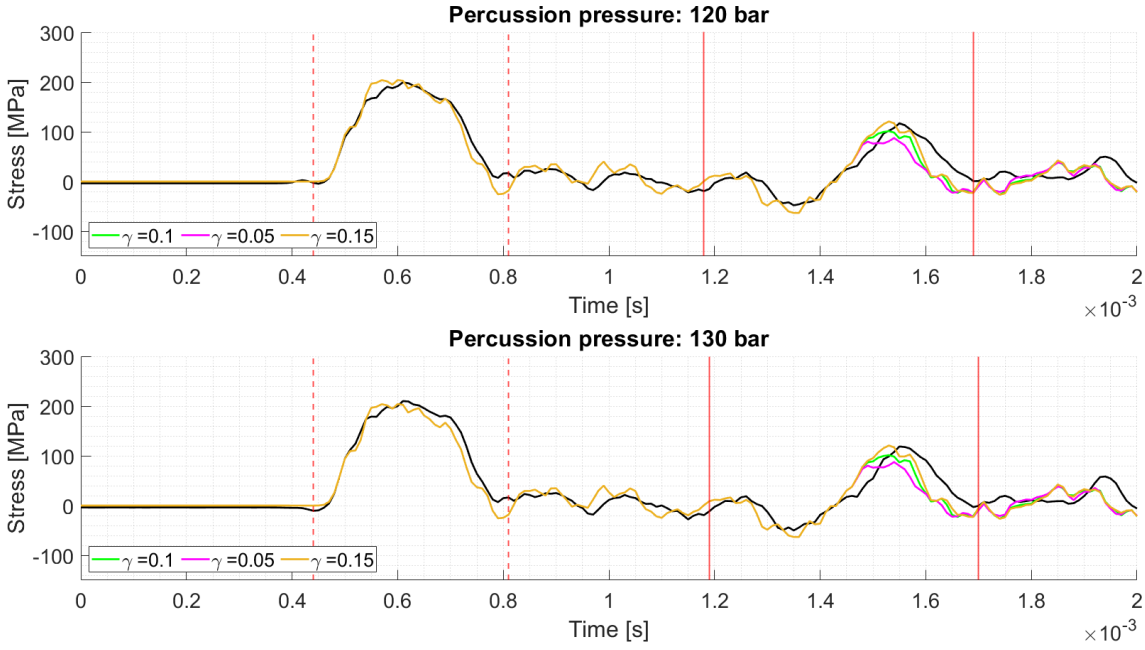

Figure 25. Differentiating unloading ratio γ with Software A at 120 bar and 130 bar percussion pressures.

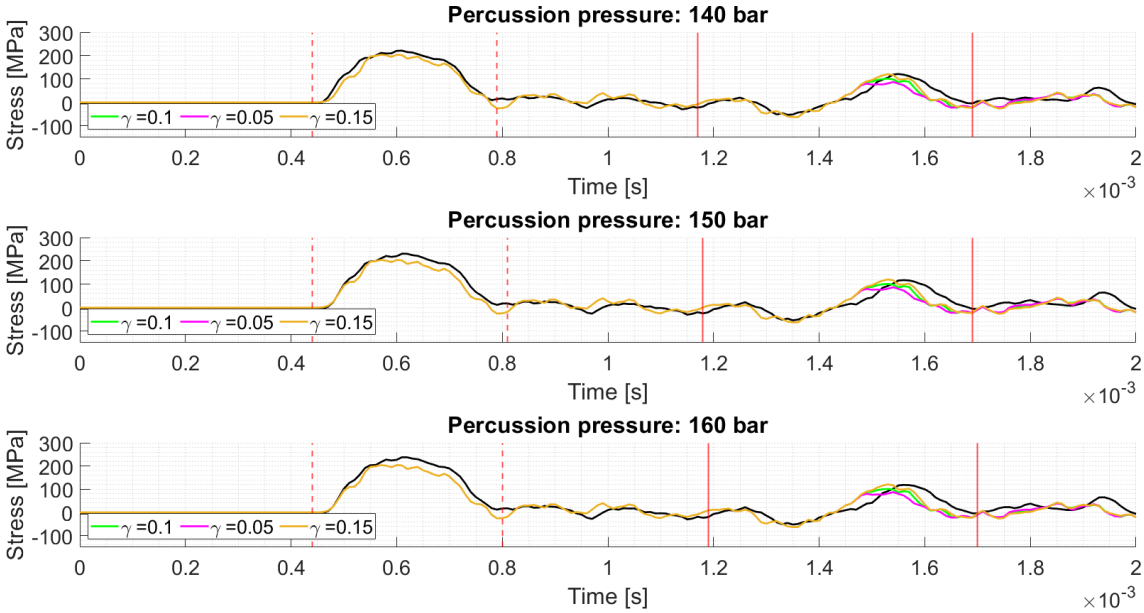

Figure 26. Differentiating unloading ratio γ with Software A at 140 bar, 150 bar, and 160 bar percussion pressures.

Table 12 presents incident wave errors $RMSE_i$ and reflected wave errors $RMSE_r$ for different γ ratios from 120 bar percussion pressure simulations.

Table 12. Errors at percussion pressure 120 bar with different unloading ratios γ.

γ	$RMSE_i$ [MPa]	$RMSE_r$ [MPa]
0.05	15.88	31.61
0.10	15.88	28.08
0.15	15.88	25.75

Table 13 shows the respective results of the correlation analysis where C_i is the incident wave correlation and C_r the reflected wave correlation with measurement mean.

Table 13. Correlations at percussion pressure 120 bar with different unloading ratios γ.

γ	C_i	C_r
0.05	0.984	0.877
0.10	0.984	0.895
0.15	0.984	0.913

5.3.2 Varying density and Young's modulus

In Figure 27, the results of two different Software B simulations are shown. The first simulation uses Young's modulus $E = 210$ GPa whereas the second simulations uses Young's modulus of 206 GPa. Both of models use a density ρ of 7800 kg/m^3. With Equation (21), calculated speeds of sound are 5189 m/s and 5139 m/s, for $E = 210$ GPa and $E = 206$ GPa, respectively. Even though the simulations are in-phase for the incident stress waves, there is a noticeable shift in phase due to different speeds of sound at a later stages of the simulations. At the end of the simulations, the signal for $E = 210$ GPa is 10 μs ahead of the $E = 206$ GPa signal. The $RMSE$ between the full simulations with $E = 210$ GPa and $E = 206$ GPa is 5.89 MPa.

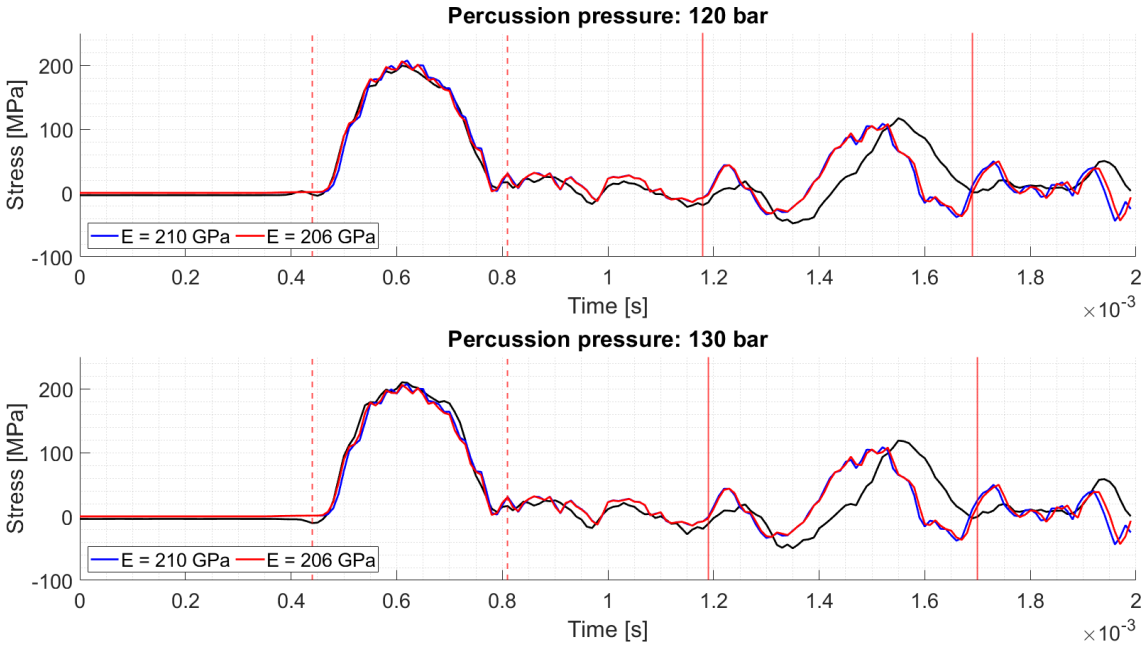

Figure 27. Software B simulation with 210 GPa and 206 GPa Young's modulus.

Figure 28 illustrates a similar case as in Figure 27 but the simulations in Figure 28 are carried out with Software A where both the density ρ and Young's modulus E are changed at the same time. For one simulation $\rho = 7800$ kg/m^3 and $E = 210$ GPa are used whereas the other uses $\rho = 7881$ kg/m^3 and $E = 200$ GPa. The speeds of sound for these simulations are 5189 m/s and 5038 m/s, respectively. Both simulations in Figure 28 use $k_1 = 350$ MN/m and $\gamma = 0.1$.

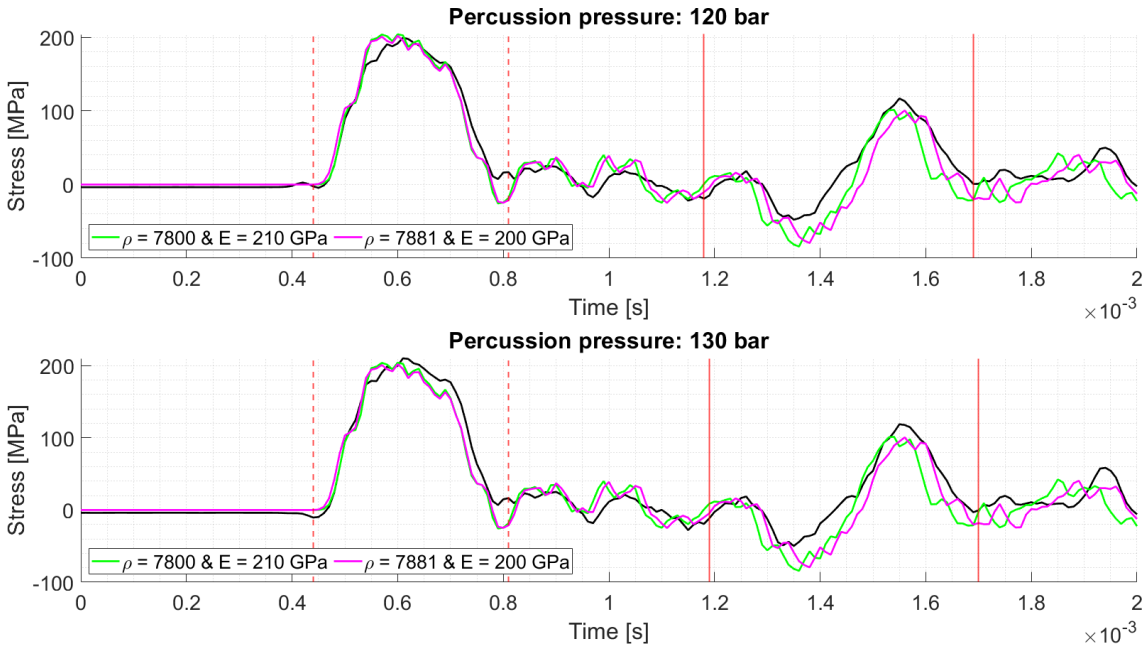

Figure 28. Software A simulation with two different densities and Young's modulus.

At the end of the simulations in Figure 28, the change in the speed of sound results in signal with higher velocity to be 40 μs ahead of the other simulation. When calculating the $RMSE$ between these two signals for the whole duration of the simulation, the error corresponds to 15.07 MPa. For comparing the two simulations to the mean measurement, Table 14 shows separate errors for incident and reflection.

Table 14. Incident and reflection errors for percussion pressure 120 bar.

ρ [kg/m^3]	E [GPa]	c [m/s]	$RMSE_i$ [MPa]	$RMSE_r$ [MPa]
7800	210	5189	15.88	31.43
7881	200	5038	15.85	28.31

5.3.3 Direction of the stress wave

Figure 29 presents a more comprehensive plot of the simulation results already shown in Figure 20. Figure 29 provides the additional information about the direction of the stress wave. A positive direction corresponds to stress wave travelling towards the drill, while a negative direction corresponds waves travelling towards the rock. Nearly all stresses in the incident wave travel in negative direction towards the rock. The part of the simulation

when stress wave is reflecting back mainly consists of stresses that travel in positive direction towards the drill but there is stress up to 18 MPa travelling the opposite direction as tensile stress.

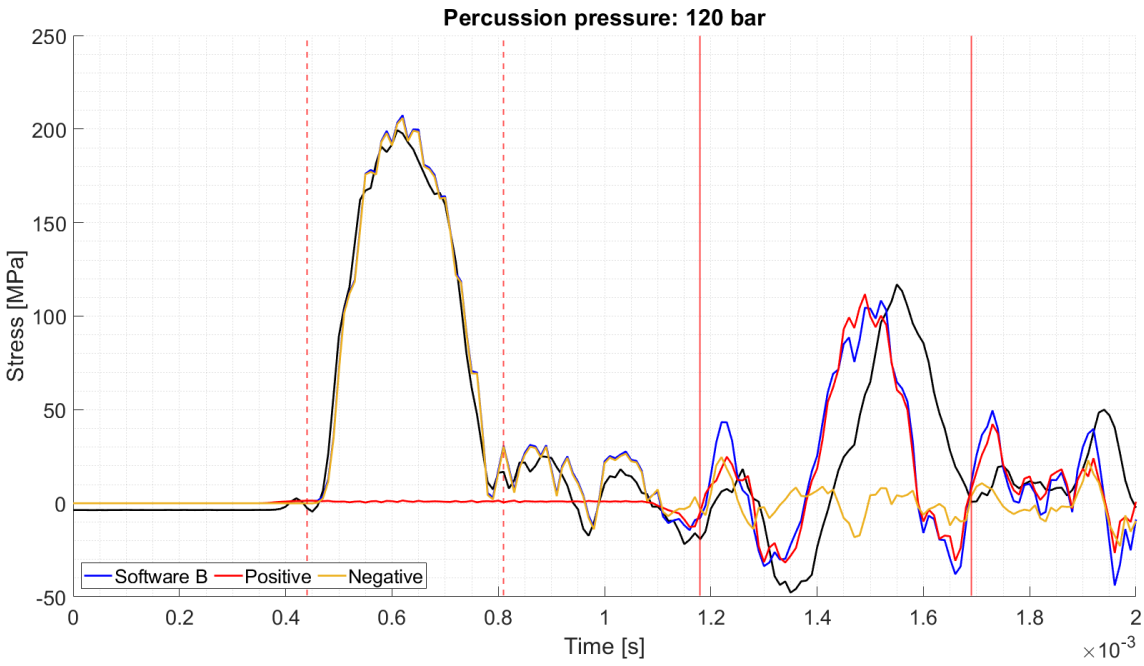

Figure 29. Direction of stress wave simulation with Software B.

5.4 Numeric simulation model of system with B thread

Figures 30 and 31 show Software B simulation results and mean measurements of B threaded system at 140 bar, 160 bar, 180 bar, and 200 bar percussion pressures.

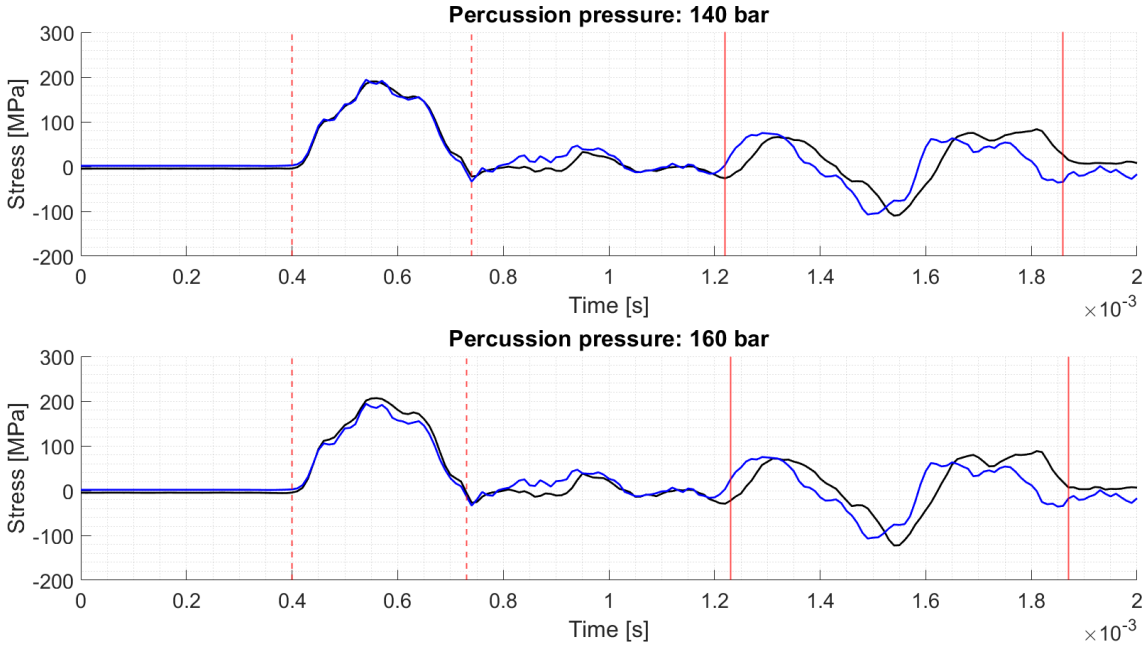

Figure 30. B threaded system stress wave simulation with 140 bar and 160 bar percussion pressures.

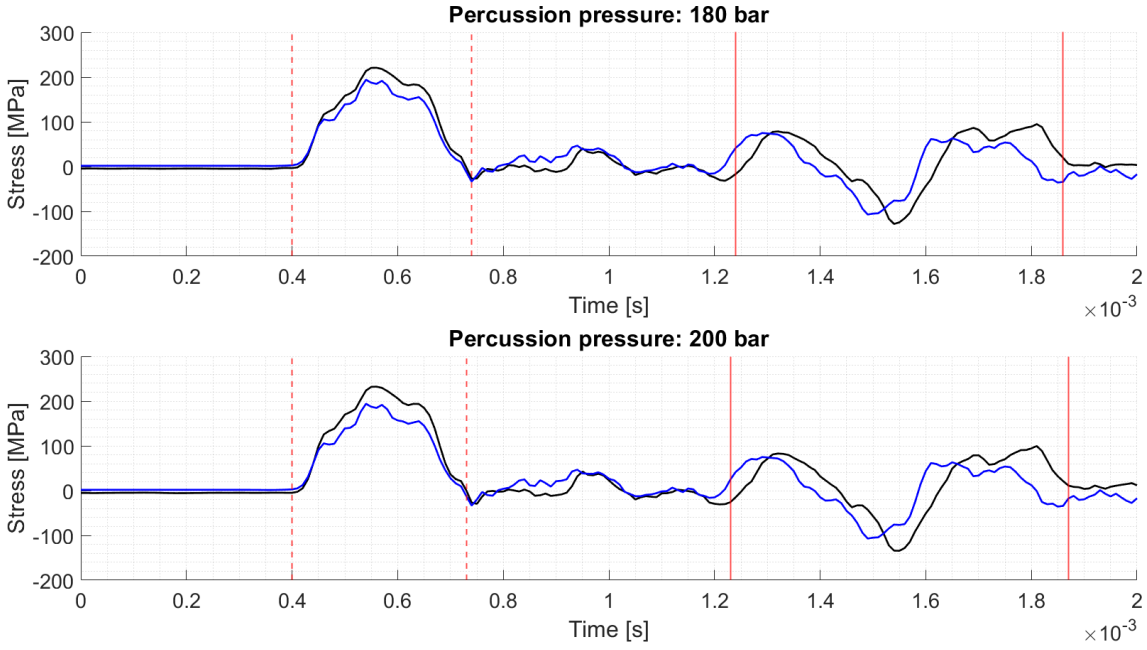

Figure 31. B threaded system stress wave simulation with 180 bar and 200 bar percussion pressures.

Table 15 contains $RMSE$s for both incident and reflected wave with an increasing percussion pressure. The lowest errors are achieved by having percussion pressure set to 140 bar.

Table 15. B threaded system stress wave simulation errors depending on percussion pressure.

p_p [bar]	$RMSE_i$ [MPa]	$RMSE_r$ [MPa]
140	5.91	48.27
160	14.30	50.88
180	23.16	53.24
200	31.65	55.57

Table 16 shows the correlations for the B threaded system stress wave simulations with measurement data. Even though $RMSE_i$ errors significantly increase for higher pressures, C_i correlations in Table 16 barely change.

Table 16. B threaded system stress wave simulation correlations depending on percussion pressure.

p_p [bar]	C_i	C_r
140	0.996	0.713
160	0.995	0.704
180	0.994	0.708
200	0.994	0.673

5.4.1 Additional drilling rod

Figures 32 and 33 show mean stress wave measurements from a drilling system where the strain gauge drilling rod is 14 ft and the second one is 12 ft. Measurements are conducted with 140 bar, 160 bar, 180 bar, and 200 bar percussion pressures.

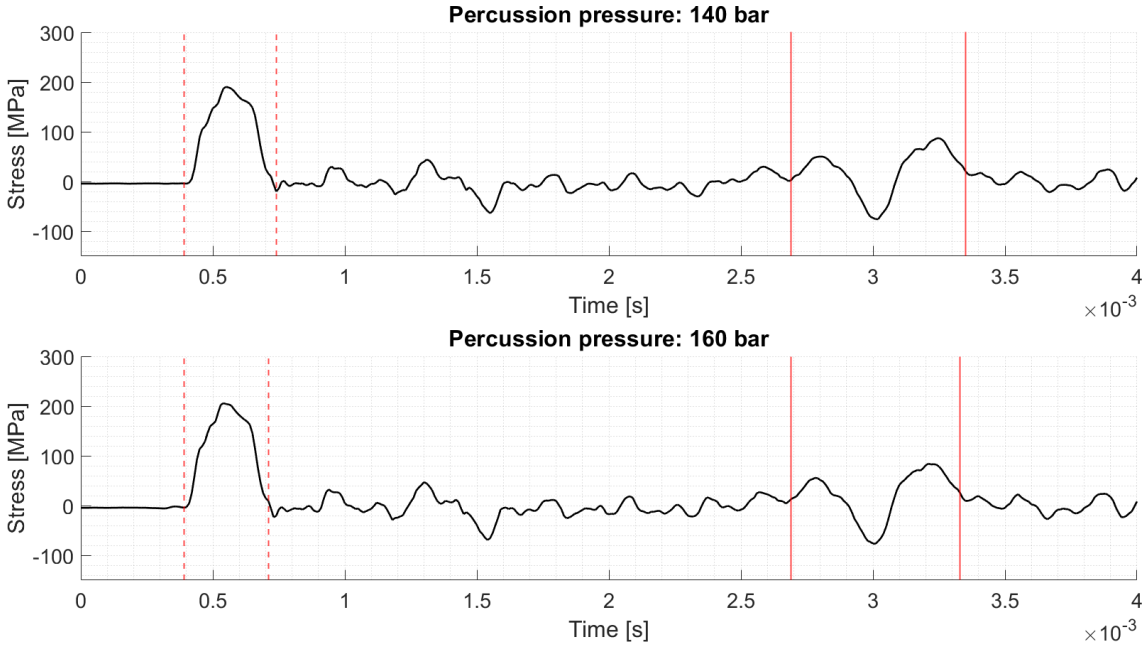

Figure 32. Two drilling rod B threaded mean stress waves with 140 bar and 160 bar percussion pressures.

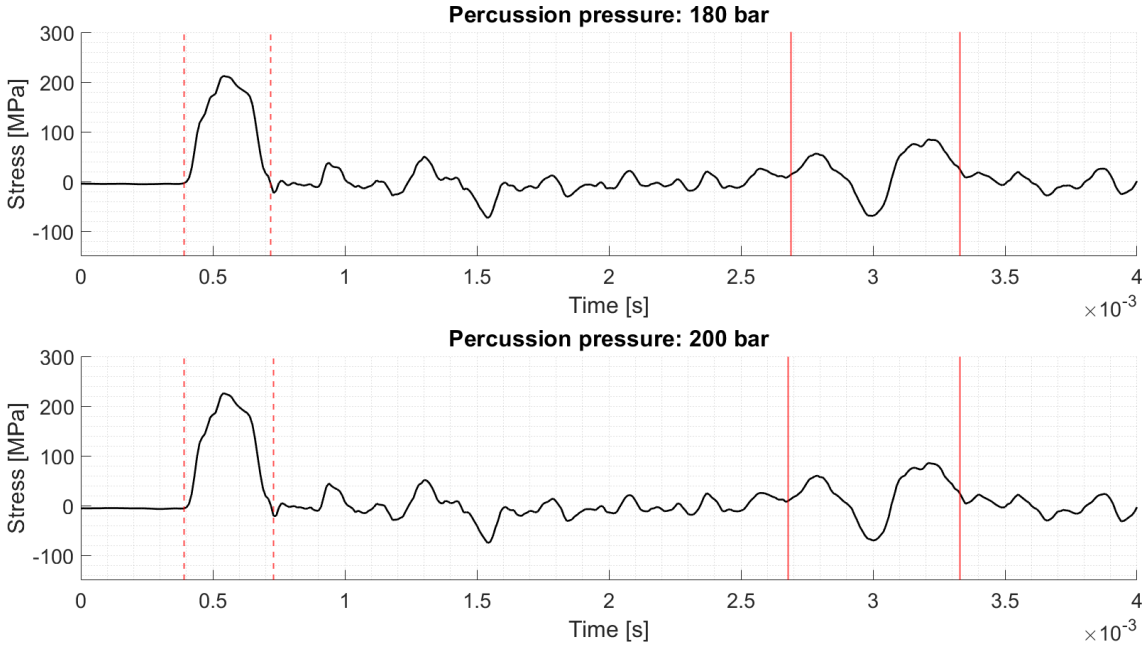

Figure 33. Two drilling rod B threaded mean stress waves with 180 bar and 200 bar percussion pressures.

Table 17 shows stress amplitudes from the mean measurements shown in Figures 32 and 33. Table 17 contains the maximum compressive stresses of incident and reflection waves and the highest tensile stress in the reflection wave. The corresponding stress wave energies and their efficiencies are shown in Table 18.

Table 17. Two drilling rod B threaded measurements' mean stress amplitudes with respect to percussion pressure.

p_p [bar]	max(σ_i) [MPa]	min($\sigma_{r,t}$) [MPa]	max($\sigma_{r,c}$) [MPa]
140	190.40	-75.67	87.18
160	205.85	-76.66	84.11
180	212.29	-69.01	85.05
200	226.05	-70.24	85.80

Table 18. B threaded measurements' mean energies with respect to percussion pressure.

p_p [bar]	$E_{\sigma,i}$ [J]	$E_{\sigma,r}$ [J]	η
140	338.25	87.58	0.741
160	399.31	88.73	0.778
180	434.29	87.23	0.799
200	483.84	89.57	0.815

When simulating a rock drilling system that uses multiple drilling rods, the numerical model must be adjusted accordingly for it to be identical with the system used in measurements. Results from a numerical model for the measurements shown in Figures 32 and 33 are shown in Figures 34 and 35.

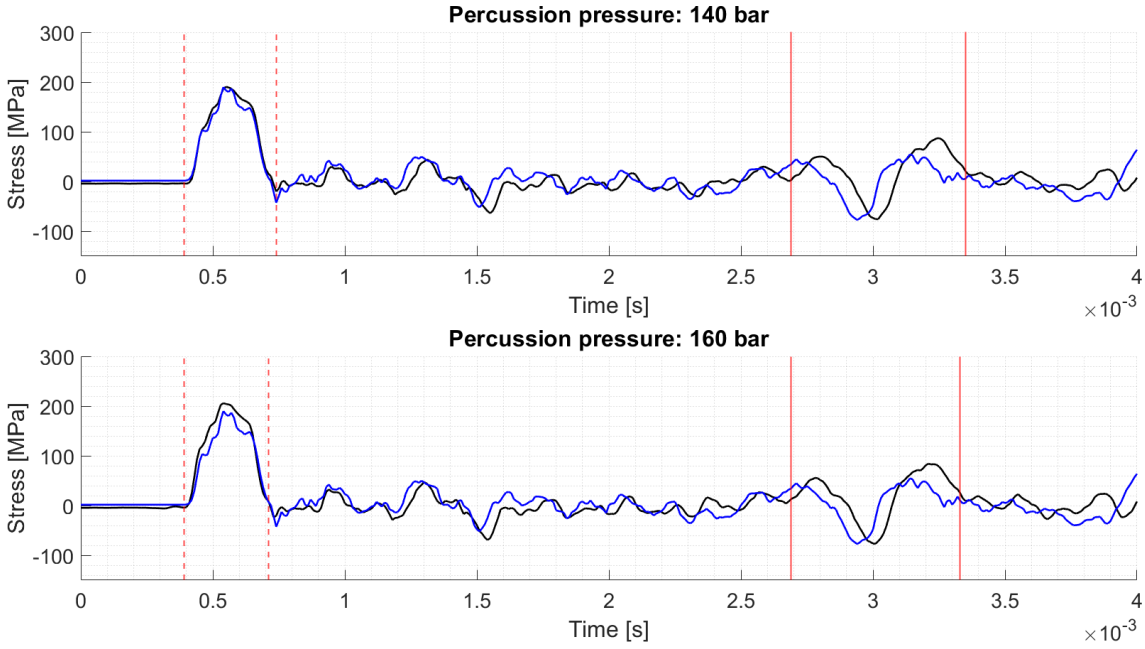

Figure 34. Two drilling rod B threaded stress wave simulation with 140 bar and 160 bar percussion pressures.

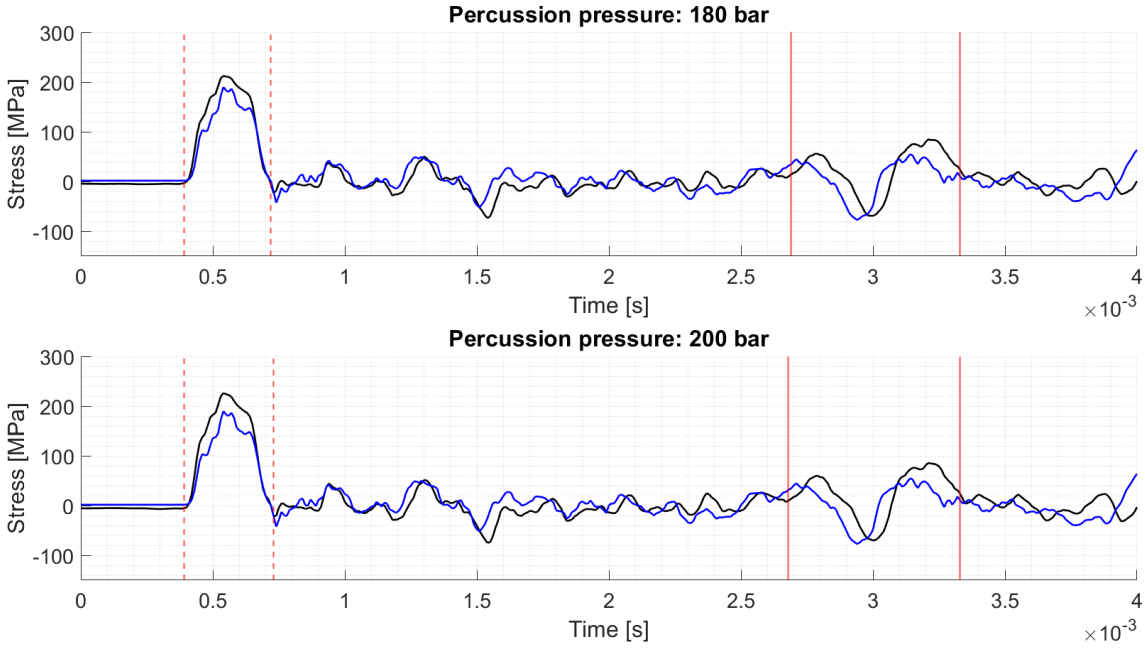

Figure 35. Two drilling rod B threaded stress wave simulation with 180 bar and 200 bar percussion pressures.

The performance of a Software B numerical model is illustrated in Tables 19 and 20. Table 19 focuses on incident wave $RMSE_i$ error and reflected wave error $RMSE_r$, while Table 20 lists the correlations C_i and C_r. When comparing errors in Table 19 with Figure 34, it can be seen the error in reflection $RMSE_r$ is caused by the fact that the signals are not in-phase. In fact, the simulation is 40 μs ahead of the measurement signal at the beginning of the reflection.

Table 19. Two drilling rod B threaded stress wave simulation errors depending on percussion pressure.

p_p [bar]	$RMSE_i$ [MPa]	$RMSE_r$ [MPa]
140	10.65	49.59
160	23.67	43.55
180	28.20	42.03
200	34.88	43.10

Table 20. Two drilling rod B threaded stress wave simulation correlations depending on percussion pressure.

p_p [bar]	C_i	C_r
140	0.994	0.528
160	0.980	0.674
180	0.983	0.709
200	0.987	0.692

5.5 Phase-shift analysis

To improve the analysis of the reflected stress wave shape and amplitude, the mean measurement signal from Figure 30 is shifted by -40 μs. The result is shown in Figure 36, where the incident wave is not in-phase in contrast to the reflection is.

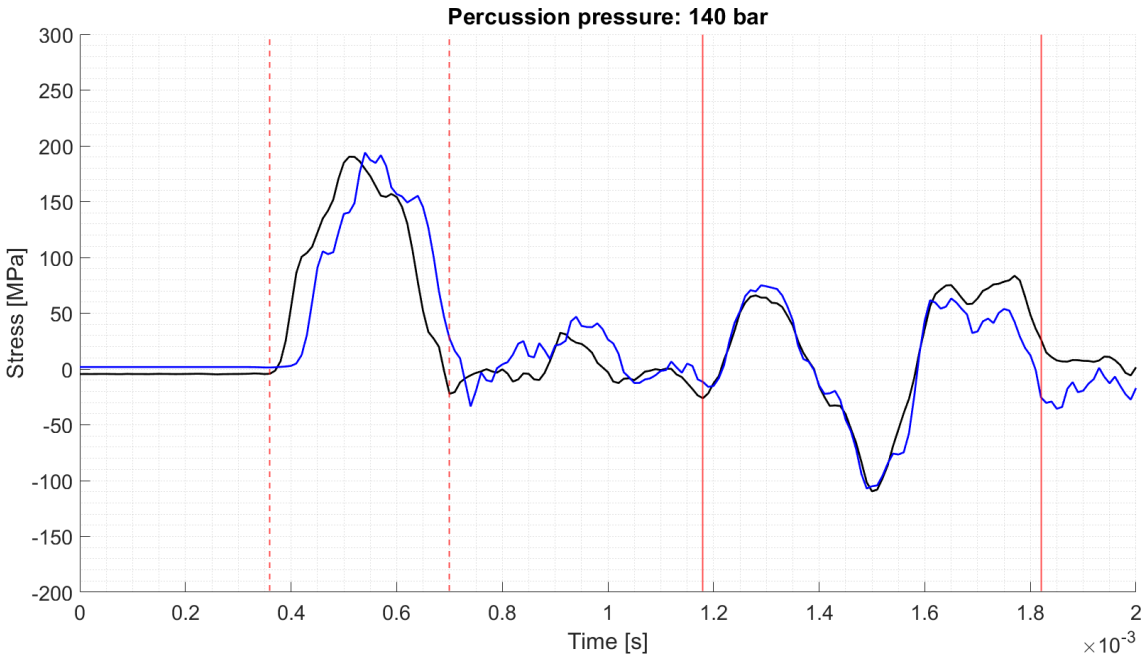

Figure 36. Stress wave reflection synchronization for B threaded measurement at 140 bar percussion pressure.

For comparing performance parameters between a signal that is in-phase with the incident wave and a signal that is in-phase with the reflection, Table 21 lists errors and correlations for both cases.

Table 21. Performance parameters of phase-shift analysis.

	$RMSE_i$ [MPa]	$RMSE_r$ [MPa]	C_i	C_r
Incident in-phase	5.91	48.27	0.996	0.713
Reflection in-phase	47.49	21.15	0.743	0.970

Because the distance that the stress waves travel in Figure 36 are equal for both signals, and since it is possible to synchronize either incident or reflection, the speeds of sound must be different between the signals. The real speed of sound of measurement signal is

$$c_{sg} = \frac{c_{sim} t_1}{t_1 - \Delta t_e} = \frac{s c_{sim}}{c_{sim} \Delta t_e + s} = \frac{4.47 \text{ m} \cdot 5189 \text{ m/s}}{5189 \text{ m/s} \cdot 40 \cdot 10^{-6} \text{ s} + 4.47 \text{ m}} = 4959 \text{ m/s},$$

where Δt_e is the time difference error after the stress wave has travelled $s = 4.47$ m. This is the time from the sensor to the bit and back to the sensor. The relative error between measurements' velocity and simulations' velocity is

$$\frac{\mid 5189 - 4959 \mid \text{m/s}}{4959 \text{ m/s}} = \frac{230}{4959} = 4.64\ \%.$$

If a similar phase-shift analysis is done for simulations results shown in in Figure 34 for the system using two 14 ft rods yields a time difference Δt_e of 70 μs. By shifting the measurement mean in Figure 34 by -70 μs, the reflected stress waves are in-phase as in Figure 37.

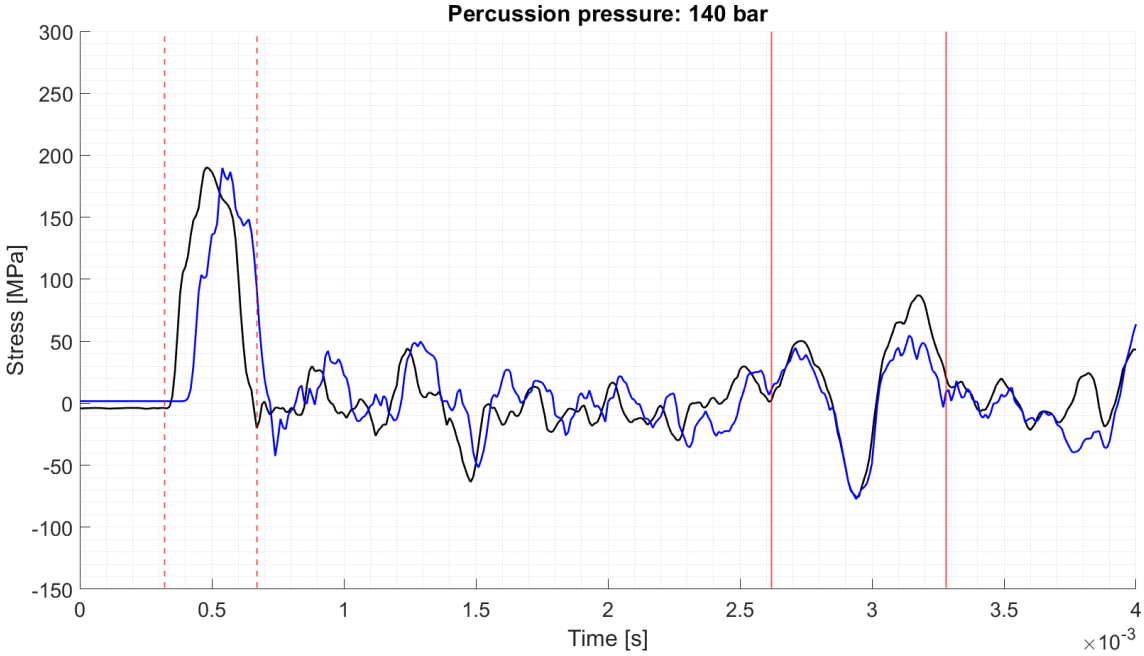

Figure 37. Stress wave reflection synchronization for B threaded two rod measurement at 140 bar percussion pressure.

By introducing an additional drilling rod that is 12 ft long, the length s that stress wave propagates between the strain gauge and the bit s increases from 4.47 meters to 11.78 meters with a factor of 2.64, while the time difference Δt_e increases from 40 μs to 70 μs with a factor of 1.75. Hereby, the speed of sound of the mean measurement in Figure 37 can be calculated to

$$c_{sg} = \frac{11.78 \text{ m} \cdot 5189 \text{ m/s}}{5189 \text{ m/s} \cdot 70 \cdot 10^{-6} \text{ s} + 11.78 \text{ m}} = 5034 \text{ m/s},$$

and the relative error is

$$\frac{\mid 5189 - 5034 \mid \text{m/s}}{5034 \text{ m/s}} = \frac{155}{5034} = 3.08 \ \%.$$

6 DISCUSSION

6.1 Current study

The numerical models described in Section 4 are designed and created by collaborators at Sandvik. My contribution in this thesis is to analyse and interpret the results from these numerical models for further use cases.

One of the first things that can be concluded from the strain gauge measurements is that the percussion pressure has an impact on the incident stress wave. With increasing percussion pressure, the incident stress wave amplitude and energy increase. While the percussion pressure affects the incident wave, there is a low correlation with reflected stress wave amplitudes or energies. It is possible to achieve higher stress wave efficiencies by increasing the percussion pressure. However, if the energy of the incident wave is high and there is a poor contact with the rock, the reflected wave energy can be too high for the system to handle without breakage.

After representing the fundamental measurement data of a drilling system that uses A thread, the initial numerical models are computed with Software A and Software B. Both models are identical to each other by having same geometries, material properties and starting values. For percussion pressures of 120 bar and 130 bar shown in Figure 20, the models tend to simulate the incident stress wave well with a lowest $RMSE_r$ of 12.16 MPa with model implemented in Software B. Even though low errors are achieved for the incident wave, there are major differences in the reflected waves. While both simulations are in-sync with the measurement mean's incident wave, the shape of the reflected waves do not correspond to the measurement. In general, the simulations do not reproduce as low tensile stresses as measured during reflection wave. In addition, the numerically simulated reflection waves have their peak compressive stresses at different times compared to the measurement means.

For conducting the analysis of the reflected wave, Section 5.3.1 includes various numeric simulations that use different bit-rock interface models. The first aspect is to run simulations where only the spring constant k_1 changes. As seen in Figures 22 and 23, changing the value of k_1 affects the shape of reflected stress wave — especially, the amplitude of tensile stress increases with decreasing k_1. Also, the amount of tensile stress affects on how soon the stress becomes compressive. From six different k_1 simulations with Software A, the lowest error $RMSE_r$ is achieved for $k_1 = 350$ MN/m. From the point of

correlation, with the same k_1, the reflection correlation $C_r = 0.934$.

Another benefit of running simulations with different k_1 is that the beginning of the reflected wave can be extinguished more clearly. As seen in Figure 24, the simulations start to deviate from each other at specific point of time. Since the simulations differ from each other only by the bit-rock interface's spring constant k_1, the point of deviation must be where the reflection starts. By comparing the point of deviation to the reflected wave annotation in Figure 24, the time difference is 10 μs.

In addition to different value of k_1, the unloading parameter γ is analysed by running simulations with $\gamma = [0.05, 0.1, 0.15]$. Since $k_2 = k_1/\gamma$, the unloading parameter γ determines the magnitude of the unloading spring constant k_2. As demonstrated in Section 3.2.4, that greater unloading spring constant k_2 leads to the dampening of the reflected forces and thereby reflected stresses.

To put it in short, it seems that when having a bilinear bit-rock interface, k_1 can be used to control the reflected wave's tensile stress amplitude which then also affects the time when the compressive part reaches the location of the sensor — while, k_2 can be used to adjust the magnitude of the compression.

Section 5.3.2 takes an aspect of adjusting Equation (23), the speed of sound. Figure 27 has the results from the first adjustment where the original Young's modulus is lowered from 210 GPa to 206 GPa. By lowering the Young's modulus, the speed of sound decreases from 5189 m/s to 5139 m/s. The difference in the speed sound results in a linearly increasing phase difference. When calculating $RMSE$ between these two simulations for the whole time span, the error corresponds to 5.89 MPa.

Figure 28 analyses the influence of the speed of sound by increasing density and decreasing Young's modulus simultaneously. When density increases from 7800 kg/m^3 to 7881 kg/m^3 and Young's modulus decreases from 210 GPa to 200 GPa, the resulting speed of sound is 5038 m/s which is 2.9 % slower than the initial one. When reading from the end of the graphs in Figure 28, the phase difference is 40 μs and this leads to $RMSE$ of 15.07 MPa between the two simulations. In terms of distance travelled, such a phase difference corresponds to 5189 m/s $\cdot\, 40 \cdot 10^{-6}$ s $= 0.2076$ m. While the reflected waves errors to the experimental data mean $RMSE_r$ are 31.43 MPa and 28.31 MPa for the faster and the slower propagations, respectively. It is important to keep in mind that the system uses only a single 12 ft drilling rod instead of multiple ones which would lead into higher phase differences.

For analysing the direction in which the stress waves propagates, Figure 29 presents separated stresses that either move towards the rock or the drill. It is worth noting that while nearly all stress in the incident wave propagate towards rock, the reflected wave consists of waves propagating both ways. Interestingly the bit reflection seen in Figure 29 at 1.225 ms, the mean measurement's reflected stress wave correlates better with the simulation that only propagates towards the drill and not the one which consists of both components.

Moving on to the B threaded system that has several differences in geometry when comparing to the A threaded system — these differences are shown in Table 1. Even though the strain gauge rod length is not the same for these two systems, the shape of the stress wave can be compared as in Figure 19, where both system's mean measurements at 140 percussion pressure is shown. When comparing the measurements shown in Figure 19, a noticeable difference can be seen for both the incident wave and the reflected wave. In terms of the incident wave, the A threaded system experiences a 42.6 joules of higher energy according to Tables 5 and 7. Similarly, the reflected wave of the A threaded system contains 44.2 joules less energy making it theoretically more energy efficient. On the other hand, it is good to keep in mind that the B threaded system has a significantly larger drill bit.

Taking a closer look at the reflected waves as shown in Figure 19, it can be seen that the B threaded system experiences twice as much tensile stress than the A threaded system. While one could hypothesise that there must have been either a poor contact with the rock or the rock itself must have been softer. But as numeric simulation in Figure 36 has neither of these issues — since the model itself is otherwise identical to the A threaded system except for the changes in geometry — the hypothesis could be rejected. Also, when comparing the bit reflections in Figure 19, there is a noticeable difference between A and B threaded systems. The difference in the bit reflections can be caused by the larger drill bit seen in the B threaded system.

After running a numeric simulation for the B threaded system as shown in Figure 30, it can be seen how well the incident stress wave correlates with the mean measurement at 140 bar percussion pressure — reaching $C_i = 0.996$ and $RMSE_i = 5.91$ MPa. On the other hand, the simulated reflection is far from being in-phase with the measurement mean. Similar results can be seen by coupling additional 12 ft drilling rod to the system in Figure 34, making the system 26 ft long in total. With the longer system, the performance corresponds to $C_i = 0.994$ and $RMSE_i = 10.65$ MPa.

With the phase difference issues seen various of numerical simulations, Section 5.5 conducts an analysis where the reflected stress waves are time shifted to be in-phase with the measurement means. By shifting the measurement mean in Figure 30 by -40 μs, $RMSE_r$ decreases from 48.27 MPa to 21.15 MPa and C_r increases from 0.713 to 0.970. Similarly, if the measurement mean in the 26 ft long system in Figure 34 is shifted by -70 μs, the reflected stress waves are in-phase. Interestingly, having additional length that the wave has to propagate does not directly proportionally increase the time difference error which might be a sign of dispersion that affects the wave propagation. Given that distance s, speed of sound in the simulation c_{sim} and time difference error Δt_e are known, the speed of sound experienced in strain gauge measurements c_{sg} can be calculated. For shorter and longer systems, the velocities c_{sg} are 4959 m/s and 5034 m/s, respectively — in terms of relative error, these correspond to 4.64 % and 3.08 %. Even though the relative errors between the velocities are not higher than 5 %, having non-matching velocities results in having signals to be out-of-phase and thereby providing significantly worse performance for the reflected wave.

To answer the research question of whether simulated models can be calibrated to be accurate as the strain gauge measurements, there is no definite answer to that. For simulating the incident stress waves even with differentiating geometries, the numerical simulations are a valid option for understanding how much energy is transferred to the rock. The most questionable aspect in using numerical models is the fact of having a fixed rock model that might be impractical to solve due to ever-changing rock conditions, which affects the state of the mass–spring–model.

6.2 Future work

While this Master's Thesis has proven to show results that can be used both to understand how stress waves are used in percussion drilling and how a more modern approach of numerically simulating these stress waves could be utilized, there is still plenty of room for future work.

One of the first tasks is to solve the phase difference issue where the simulation's reflected wave is not in-phase with the measurement mean if the incident waves are in phase. While the issue is likely caused by incorrect speed of sound used in the model, it should be researched whether the phase difference linearly increase with increasing amount of the drilling rods. In case where the phase difference does not linearly increase with longer system, it is possible that for example the couplings can create dispersion that affects

frequency and thereby the speed of sound. It is also worth studying how much density and Young's modulus can deviate within in the tool materials.

While synchronizing incident and reflected waves might be straightforward to investigate and solve, conducting thorough analysis for the rock's behaviour as a continuously changing elastic object can be found challenging to model. With this thesis' results, it can be concluded how a bilinear rock model performs and what changes can be seen from the results with different parameters. Another thing to consider when trying to improve the rock model, would be to use a trilinear model or a model that would be a combination of linear and nonlinear stiffnesses.

As a final aspect for future work, differentiating the directions of the stress wave propagation could render a crucial means to improve the agreement of the numerical simulation results with the measurement data, as the reflected wave is a mixture of stresses that propagate in opposite directions.

7 CONCLUSION

FEM can be used to numerically approximate stress wave propagation in a rock drilling system. One of the key characteristics that the numerical simulations are good at is the ability to adapt to geometry changes in the system. Since the incident stress wave solely depends on what happens between the piston and the strain gauge, it is feasible to simulate the incident wave if the model is prepared accurately. The reflected wave however, depends on the incident wave, system geometries and the rock properties, thus increasing the modelling complexity tremendously. For example, Figure 22 illustrates well the effect of having ever-changing rock conditions. Since the rock stiffness can change after each percussion cycle, it is obviously challenging to optimize such numerical model for multipurpose rock conditions. If the rock stiffness were to stay constant throughout the borehole, the presented bilinear rock model could be optimized by fine-tuning the loading and unloading spring constants that affect reflected stress wave amplitudes. Hereby, the rock model optimization is one of the decisive future works for calibrating numerical model to be as accurate as strain gauge measurements.

While the numerical models have shown to provide evident results for simulating both the incident and reflected stress waves, the models still require more tuning to be coherent with the measurements. Despite of having the incident waves of simulation and measurement in-phase, the reflected waves are consistently out-of-phase, although shapes and amplitudes of the reflected waves are well reproduced. For conducting any further research with numerical models used in this thesis, the speed of sound needs to be analysed to adapt the model specifically, while also keeping in mind that wave dispersion could also possibly affect the speed of sound.

REFERENCES

[1] Kobayashi, H., Seo, Y., Ogawa, K., Horikawa, K., & Tanigaki, K., (2018), 'Numerical Analysis and Experiment for Stress Wave Propagation in Two Connected Cylindrical Bodies with Different Cross-Sectional Area and Same Mechanical Impedance', *EPJ Web of Conferences*. 2018 Les Ulis: EDP Sciences, pp. 1033.

[2] Allaire, G. & Craig, A., (2007), *Numerical Analysis and Optimization: An Introduction to Mathematical Modelling and Numerical Simulation*, Oxford University Press, Incorporated, Oxford.

[3] Chiang, L. E. & Elías, D. A., (2008), 'A 3D FEM methodology for simulating the impact in rock-drilling hammers', *International journal of rock mechanics and mining sciences*, vol. 45, no. 5, pp. 701–711.

[4] Zhang, Z.-X., (2016), *Rock fracture and blasting : theory and applications*, Butterworth-Heinemann, Amsterdam.

[5] Zhan, H., Zhang, G., Yang, C., & Gu, Y., (2018), 'Breakdown of Hooke's law at the nanoscale - 2D material-based nanosprings', *Nanoscale*, vol. 10, no. 40, pp. 18961–18968.

[6] Li, Q., Zhao, G.-F., & Lian, J., (2019), 'A Fundamental Investigation of the Tensile Failure of Rock Using the Three-Dimensional Lattice Spring Model', *Rock mechanics and rock engineering*, vol. 52, no. 7, pp. 2319–2334.

[7] Zhao, G.-F., Fang, J., & Zhao, J., (2011), 'A 3D distinct lattice spring model for elasticity and dynamic failure', *International journal for numerical and analytical methods in geomechanics*, vol. 35, no. 8, pp. 859–885.

[8] Mansuripur, M., (2011), *The Lorentz Oscillator Mode*, Field, Force, Energy and Momentum in Classical Electrodynamics, pp. 140–162.

[9] Gross, D., Hauger, W., Schröder, J., Wall, W., & Bonet, J., (2018), *Engineering Mechanics 2 Mechanics of Materials*, 2nd ed, Springer Berlin Heidelberg, Berlin.

[10] Hopcroft, M.A., Nix, W.D., & Kenny, T.W., (2010), 'What is the Young's Modulus of Silicon?', *Journal of microelectromechanical systems*, vol. 19, no. 2, pp. 229–238.

[11] Hämäläinen, P., (2013), ‘Signaalinkäsittelyn käyttö mittausmenetelmän tehostamiseksi liikkuvissa työkoneissa’, Master’s Thesis, Tampere University of Technology.

[12] Liu, G.R., Quek, S.S., & Liu G.R., (2003), *Finite Element Method: A Practical Course*, Elsevier Science & Technology, Oxford.

[13] Rantala, E., (1997), ’Iskuporauksen dynamiikan simulointi’, Master’s Thesis, Tampere University of Technology.

[14] Graff K., (1975), *Wave Motion in Elastic Solids*, Dover Publications.

[15] Kauppinen, K., (1974), ’Kallioporakoneen iskumännän muodon optimointi’, Master’s Thesis, Tampere University of Technology.

[16] Savolainen, H., (1982), ’Niskatangon matemaattinen simulointi’, Master’s Thesis, Tampere University of Technology.

[17] Vulli, P., (1975), ’Energian siirtyminen kallioporakoneen iskumännästä kiveen’, Master’s Thesis, Tampere University of Technology.

[18] Ramamurthi, K., (2021), *Modeling explosions and blast waves*, 2nd ed, Springer, Cham.

[19] Razavi, S., Callegari, G., Drazer, G., & Cuitiño, A., (2016), ‘Toward predicting tensile strength of pharmaceutical tablets by ultrasound measurement in continuous manufacturing’, *International journal of pharmaceutics*, vol. 507, num. 1–2, pp. 83–89.

[20] Lundberg, B. & Huo, J., (2017), ‘Biconvex versus bilinear force-penetration relationship in percussive drilling of rock’, *International journal of impact engineering*, vol. 100, pp. 7–12.

[21] Chen, C., Chen, S., Zhang, Y., Lin, H., & Wang, Y., (2022), ‘A Unified Nonlinear Elastic Model for Rock Material’, *Applied sciences*, vol. 12, no. 24, pp. 12725.

[22] Lundberg, B. & Okrouhlik, M., (2006), ‘Efficiency of a percussive rock drilling process with consideration of wave energy radiation into the rock’, *International journal of impact engineering*, vol. 32, no. 10, pp. 1573–1583.

[23] Chiang, L. E., (2004), ‘Dynamic force-penetration curves in rock by matching theoretical to experimental wave propagation response’, *Experimental mechanics*, vol. 44, no. 2, pp. 167–175.

[24] Meehan, C. L. & Talebi, M., (2017), 'A method for correcting field strain measurements to account for temperature effects', *Geotextiles and geomembranes*, vol. 45, no. 4, pp. 250–260.

[25] Kalevo, N., (2012), 'Magnetoelastic properties of heat treated steels', Master's Thesis, Tampere University of Technology.

[26] Weiss, G., (1969), 'Wheatstone Bridge Sensitivity', *IEEE transactions on instrumentation and measurement*, vol. 18, no. 1, pp. 2–6.

[27] Lei, J.-F. & Will, H. A., (1998), 'Thin-film thermocouples and strain-gauge technologies for engine applications', *Sensors and actuators. A. Physical*, vol. 65, no. 2, pp. 187–193.

[28] Papageorgiou, S. N., (2022), 'On correlation coefficients and their interpretation', *Journal of orthodontics*, vol. 49, no. 3, pp. 359–361.

[29] Bijima, F., Jonker, M., Van der Vaart, A., & Erné, R., (2017), *An Introduction to Mathematical Statistics*, Amsterdam University Press, Amsterdam.

[30] Karunasingha, D. S. K., (2022), 'Root mean square error or mean absolute error? Use their ratio as well', *Information sciences*, vol. 585, pp. 609–629.

[31] Pianosi, F., Sarrazin, F., & Wagener, T., (2015), 'A Matlab toolbox for Global Sensitivity Analysis', *Environmental modelling & software : with environment data news*, vol. 70, pp. 80–85.

[32] Mathworks, *MATLAB*, https://www.mathworks.com/products/matlab.html, Last accessed 12 December 2022.

[33] Tkalcec, I., Azcoitia, C., Crevoiserat, S., & Mari, D., (2004), 'Tempering effects on a martensitic high carbon steel', *Materials science and engineering. A, Structural materials : properties, microstructure and processing*, vol. 387, pp. 352–356.

[34] Hussain, G., Hameed, A., Horsfall, I., Barton, P., & Malik, A. Q., (2012), 'Experimental and simulation optimization analysis of the Whipple shields against shaped charge', *Acta mechanica Sinica*, vol. 28, no. 3, pp. 877–884.

[35] Prasad, M. & XiaoBing, S., (2020), ‘Post-cracking Poisson Ratio of Concrete in Steel-Concrete-Steel Panels Subjected to Biaxial Tension Compression’, *IOP conference series. Materials Science and Engineering*, vol. 758, no. 1, pp. 12081.

[36] Depouhon, A., Denoël, V., & Detournay, E., (2015), ‘Numerical Simulation of Percussive Drilling’, *International journal for numerical and analytical methods in geomechanics*, vol 39, no. 8, pp. 889–912.

Appendix 1. Rock drilling animation

Figure A1.1 presents an animation overview of a rock drill system where the stress wave first propagates from right to left and then reflects.

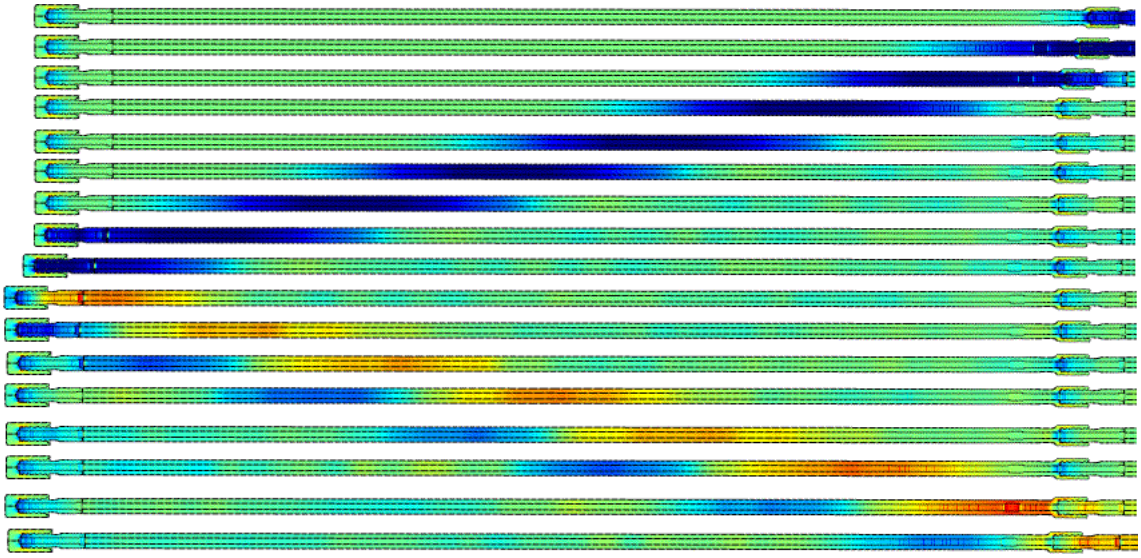

Figure A1.1. Percussion animation in a rock drill system, where blue and red colours represent zones of compression and tension, respectively.